6

Stabilization, Trim, and Control Devices

Stabilization, trim, and control devices are the prerequisites for flyability and controllability of aerospace flight vehicles. Regarding re-entry flight of RV-W's, we have mentioned in Section 2.1.2 that initially, at high altitudes, the reaction control system (RCS) is the major flight control system. Aerodynamic trim, stabilization and control surfaces take over further down on the trajectory. This is in contrast to CAV's, where aerodynamic stabilization and control surfaces are the only devices. Obviously, deploying such devices result in a strong coupling of the thrust vector (and the aerothermoelasticity of the airframe), Sub-Section 2.2.3, into the flight dynamics, trim and control of the vehicle. Moreover, for ARV's, the trajectory is such that they reach high altitudes in a situation similar to RW-V's so that control surface effectiveness eventually is diminished and reaction control systems (RCS) have to be deployed. In other words, ARV's require two different control systems. On the other hand, the capsule RV-NW's, as a rule, have only RCS for flight control.

We begin this chapter with an introduction to trim and control surface aerothermodynamics, and concentrate then on the onset flow[1] characteristics. Next treated is the asymptotic behavior of pressure, the thermal state of the surface and wall shear stress on the control surface, approximated here as a ramp. Related issues of reaction control systems are discussed briefly. Configurational considerations are presented regarding the discussed trim and control devices. Finally the results are summarized and simulation issues are examined. Our aim is to foster the understanding of the flow phenomena involved in the operation of stabilization, trim, and control devices and the problems related to their simulation with experimental and computational means.

6.1 Control Surface Aerothermodynamics, Introduction

In this and the following sections of the chapter, we concentrate on aerothermodynamic issues of trim and control surfaces. We are concerned mainly with their effectiveness. Therefore we look not only at shock/boundary layer interactions as such, which are major factors regarding especially thermal and

[1] We use the term "onset flow" for the (incoming) flow just ahead of the respective device.

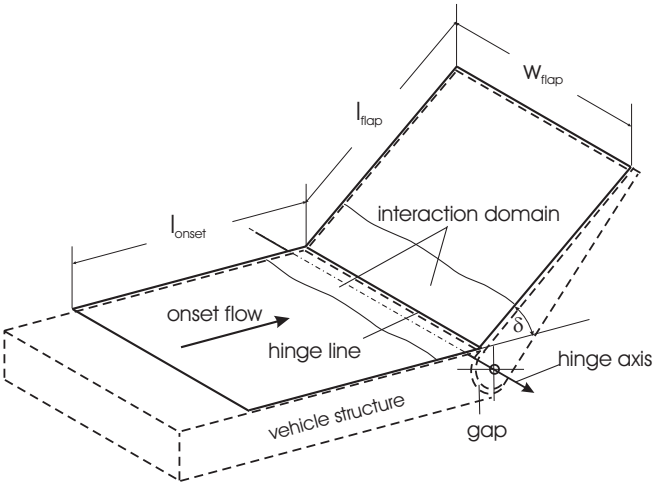

Fig. 6.1. Flat-plate/ramp configuration as generic flap configuration. We call the corner line the hinge line. Note that its location and that of the hinge axis are not exactly the same.

also mechanical (pressure and shear stress) loads on such surfaces, but also at other issues, especially at the role of the control surface onset flow. Material about shock/boundary layer interactions can be found abundantly in the literature, we point here only to [1]–[5]. Usually two-dimensional interactions are treated because they are in general the most severe ones. In reality many three-dimensional cases can be found, see, e.g., [6]–[8]. A detailed discussion of means for control of shock wave/turbulent boundary layer interaction at transonic and supersonic Mach numbers is given in [9].

We try here do develop a somewhat wider view which emphasizes also the influence of the flow ahead of a trim or control surface, i.e., the onset flow, on the effectiveness of a surface.[2] Of practical importance, too, is the "asymptotic" flow behavior on the trim or control surface, i.e., the flow behavior downstream of the strong interaction domain. In general the strong interaction domain has a small effective downstream extent compared to the flap length; therefore, it is the asymptotic behavior which mostly governs the effectiveness of a trim or control surface, Fig. 6.1.

6.1.1 Flap Effectiveness: Influence of the Onset Flow Field

In order to discuss effectiveness aspects of aerodynamic trim and control surfaces, we look at the generic flap configuration, Fig. 6.1, which consists simply

[2] Of course this is always a topic, too, when shock/boundary layer interaction is studied. However, usually the onset flow situation is that of a laboratory experiment with idealized restrictions.

of a flat plate and a ramp. As a body flap on a RV-W, for instance, it would be located upside down at the end of the vehicle's lower side.[3], see, e.g., Fig. 6.44 Of importance are the properties of the onset flow, which are different for different vehicle classes, depending on flight speed, altitude, vehicle shape and attitude, and on the thermal state of the surface. We consider the overall properties of the onset flow, and in addition the influence of the important similarity and geometrical parameters. Geometrical parameters are the ramp (deflection) angle, the hinge line orientation (basically we consider the optimum case of orientation: orthogonal to the onset flow), the width and length of the flap (ramp), and the width of the gap between the vehicle parent structure and the flap. Before we begin with the consideration of the overall onset flow in Section 6.2, we look at the particular flap deflection modes in hypersonic flight.

6.1.2 Flap Deflection Modes during Hypersonic Flight

During re-entry of a RV-W at large angle of attack, the body flap as the main trim surface, as well as the elevator and aileron surfaces, Fig. 6.44, usually are deflected downwards, Sub-Section 3.4.2. Negligible pressure forces are generated at the lee surfaces due to the hypersonic shadow effect [10]. Upward deflection does not yield aerodynamic forces because the body flap is in the shadow of the fuselage and the elevons are in the wing's shadow. However, upward deflection of a surface does have an effect on the moment balance of the vehicle, because now the (upward) force acting on the initially downward deflected or undeflected lower surface is reduced or even omitted completely, Sub-Section 3.4.2.

A shadow effect, either the hypersonic one, or simply one due to massive flow separation, exists at large angle of attack for a central single vertical tail unit (stabilizer) together with the rudder, Fig. 6.44a). On the re-entry trajectory, down to rather small angles of attack, it will first be subjected to the hypersonic shadow effect, and then lies in the separated flow domain above and behind the fuselage, Sub-Section 2.1.2. At small angles of attack, the vertical stabilizer and the deflected rudder are effective as long as the yaw angle of the vehicle is not too large. Otherwise, there is also a shadow effect. Regarding vertical wing-tip stabilizers and rudders, Fig. 6.44b), the effectiveness of the surfaces will also suffer from shadow effects at large angles of attack or yaw.

We do not encounter the above mentioned problems for CAV's which fly at small angles of attack. The effectiveness of their stabilization, trim and control surfaces, Fig. 6.46, is not reduced by shadow effects of either kind. Of course, like for low speed aircraft, angle of attack and yaw have an influence, because in principle they alter the properties of the onset flow, however, in a well understood manner.

[3] The deflection angle η of horizontal surfaces in aerodynamics usually is counted positive when deflected downwards.

For both RV-W and CAV's, aerothermoelasticity of the airframe and, in particular, of stabilization, trim and control surfaces with large mechanical and thermal loads can be a special problem. Although the effects of aerothermoelasticity are a major problem in hypersonic flight-vehicle design, we cannot treat them in the frame of this book. However, we discuss aspects of them in Chapter 8.

6.2 Onset Flow of Aerodynamic Trim and Control Surfaces

6.2.1 Overall Onset Flow Characteristics

To understand the aerothermodynamic phenomena and the thermal and mechanical loads present at a trim or control surface, the properties of the overall onset flow, together with the thermal state of the surface, need to be considered first.

Regarding the body flap and the elevator/aileron surfaces of a RV-W, the onset flow on a large part of the trajectory is governed by the high angle of attack and the very blunt body shape, Figs. 6.2b) and 3.1. The topology of the onset flow field itself at the windward side is also important, Sub-Section 3.2.2. The situation is different for a CAV, Fig. 6.2a), where the slender configuration flies at small angle of attack and the onset flow of the elevator/aileron surfaces does not deviate very significantly from the free-stream flow. The flow topology of the wing's lower and upper side are also important, Sub-Section 4.2.2.

In order to illustrate the different flow situations over RV-W's and CAV's, we compare the lower-side onset flow data for four flight cases using the RHPM (Rankine-Hugoniot-Prandtl-Meyer) configurational approximation, Section 10.1. The first two are those of a body flap surface of a typical RV-W (Space Shuttle Orbiter, Sub-Section 3.3.1, however without boattailing) at $M_\infty = 24$ and $H = 70$ km with laminar flow (RV-W 1), and at $M_\infty = 6$ and $H = 40$ km with turbulent flow (RV-W 2). The other two are those of elevator/aileron surfaces of a typical CAV (CAV 1, ramjet propulsion) at $M_\infty = 6.8$

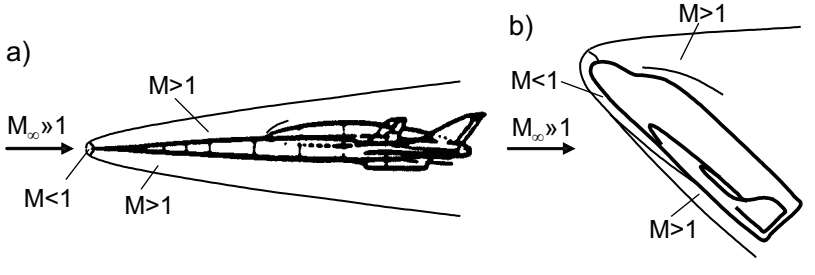

Fig. 6.2. Schematic of configurations, angles of attack and bow shock shapes of a) CAV, and b) RV-W [10].

Table 6.1. Flight parameters of the four cases: RV-W 1 and RV-W 2: RV-W-type vehicle (Space Shuttle Orbiter without boattailing), CAV 1: CAV-type vehicle with ramjet propulsion (SÄNGER lower stage), CAV 2: CAV-type vehicle with scramjet propulsion.

Flight vehicle:	RV-W 1	RV-W 2	CAV 1	CAV 2
M_∞ [-]	20	6	6.8	12
H [km]	70.0	40.0	30.0	34.2
α [°]	40.0	25.0	5.0	5.0
L_{ref} [m]	32.0	32.0	82.0	20.0
T_∞ [K]	219.69	250.33	226.51	234.27
v_∞ [m/s]	5,942.7	1,903.1	2,051.6	3,682.0
ρ_∞ [kg/m^3]	$8.75{\cdot}10^{-5}$	$4.0{\cdot}10^{-3}$	$1.84{\cdot}10^{-2}$	$9.61{\cdot}10^{-3}$
q_∞ [kPa]	1.54	7.24	38.72	65.0
p_∞ [Pa]	5.52	287.4	1,196.4	646.27
Re^u_∞ [m^{-1}]	$3.36{\cdot}10^4$	$4.52{\cdot}10^5$	$2.39{\cdot}10^6$	$2.19{\cdot}10^6$

and $H = 30$ km (SÄNGER lower stage), and (CAV 2, scramjet propulsion) at $M_\infty = 12$ and $H = 34.2$ km. For the latter, we have assumed a rather high dynamic pressure $q_\infty = 65$ kPa. From this, we get with

$$q_\infty = \frac{\rho_\infty v_\infty^2}{2} = \frac{\gamma}{2} p_\infty M_\infty^2 \;\Rightarrow\; p_\infty = \frac{2q_\infty}{\gamma M_\infty^2} \;\Rightarrow\; H, \tag{6.1}$$

the pressure $p_\infty = 644.84$ Pa and the flight altitude[4] $H = 34.2$ km, Table B.1. The overall length of the vehicle is assumed to be $L_{ref} = 20$ m. The product of dynamic pressure q_∞ and $c_{p_{e,onset}}$, Table 6.2, a measure of the lift force, is approximately the same for the two CAV's. In Table 6.1 the flight parameters of the four vehicle cases are collected.

Under onset flow data, we understand it to mean the external (outer edge of the boundary layer) inviscid flow data immediately ahead of the control surface $(e, onset)$,[5] and also those of the attached viscous flow, which in general can be considered as being of boundary layer type. Unfortunately, onset flow data, as we wish to consider them, are not available in the literature.

[4] This is a very simple approach, the determination of a real trajectory point takes much more data into account, Section 2.2.

[5] Actually, if the entropy layer, see below, has not been swallowed by the boundary layer, the inviscid flow above the boundary layer edge has a strong gradient in direction normal to the surface, even a small velocity minimum is possible, Sub-Section 6.2.2. This flow property also has a large influence on the flap effectiveness.

In order to get estimates of the onset flow properties, we approximate the configurations with the help of the RHPM flyer. This very simple approximation in the sense of shock-expansion theory yields constant one-dimensional inviscid flow data, which we also consider as external flow data of the onset flow boundary layer. However, we choose the flat-plate situation with the extended RHPM$^+$ approach, Section 10.1, taking into account the γ_{eff} influence, and also the total pressure loss due to the bow shock. The compressibility factor is chosen to be $Z = 1$. Therefore the affected data, such as temperatures and related entities, must be considered with extra care. We understand, that the RHPM$^+$ approach is a rather crude way to estimate data. Therefore the resulting data in Table 6.2 are meant for illustrative purposes only.

The onset flow length l_{onset} which governs the onset flow boundary layer thickness, Table 6.5, was chosen to be equal to the reference length for the RV-W, where the body flap is considered. For the two CAV's, where the elevator/aileron surfaces are considered, the length from the leading-edge tip to mid-chord of the control surfaces was chosen. Although the flow situation on the lower (windward) side of a delta wing at angle of attack is complicated due to the primary attachment lines there, see, e.g., Sub-Section 3.3.2 of [10], this assumption nevertheless should serve sufficiently well.[6]

Due to surface radiation cooling that is important in all four cases, the radiation-adiabatic surface temperature is not constant [10]. It drops strongly from the forward stagnation point in the nose region towards the vehicle aft part. The same holds on the wing part of a vehicle, where it drops from the primary attachment line at the leading edge towards the wing's trailing edge. Despite this we choose for all cases a constant wall temperature and hence onset wall temperature $T_{w,onset}$, which is equal to the radiation-adiabatic temperature at the onset location. For the case RV-W 1 we choose $T_w = 1,000$ K according to data from [11] for the re-entry flight STS-2 of the Space Shuttle Orbiter. For case RV-W 2 we take $T_w = 900$ K. For CAV 1 we choose $T_w = 1,000$ K, too. Because of the shorter onset flow length of CAV 2, we take $T_w = 1,200$ K.

We discuss now some of the few data in Table 6.2. We note that in case RV-W 1 the pressure coefficient with $c_{p_{e,onset}} = c_{p_w} = 0.89$ by chance compares well with $c_{p_w} \approx 0.89$ at the pressure plateau at the lower side of the Orbiter at $M_\infty = 24$ and $\alpha = 40°$, Sub-Section 3.5.2. Our simple approach however does not yield flight Mach number and high temperature real gas effects independence, Section 3.6. The dynamic pressure of the (inviscid) onset flow, $q_{e,onset}$, represents the momentum flux and hence can be considered as a measure of the flap effectiveness. This is larger than q_∞, which is used for non-dimensionalization. Anyway, we see that $q_{e,onset}$ is small for the two RV-

[6] The reader should note, that the onset flow lengths involved in the four cases are large compared to the lengths which are found on the vertical stabilizers, either single or dual surfaces on the upper side of the airframe, or on the fins at the wing tips of the same vehicles, Sub-Section 6.6.1.

Table 6.2. Data of the lower-side inviscid onset flow (RHPM$^+$ approximation, $Z = 1$) of the body flap for the cases RV-W 1, RV-W 2, and elevator/aileron surfaces for the cases CAV 1, CAV 2. The subscript 'e' stands for boundary layer edge condition.

Flight vehicle:	RV-W 1	RV-W 2	CAV 1	CAV 2
M_∞ [–]	20	6	6.8	12
H [km]	70.0	40.0	30.0	34.2
α [°]	40.0	25.0	5.0	5.0
l_{onset} [m]	32.0	32.0	25.0	6.0
γ_{eff} [–]	1.14	1.4	1.4	1.3
θ [°]	43.66	34.28	12.06	7.71
$M_{e,onset}$ [–]	3.93	2.83	5.95	11.4
$T_{e,onset}$ [K]	3,678.3	789.18	287.22	275,34
$v_{e,onset}$ [m/s]	4,308.3	1,593.4	2,021.7	3,652.9
$\rho_{e,onset}$ [kg/m^3]	$1.31{\cdot}10^{-3}$	$1.67{\cdot}10^{-2}$	$3.17{\cdot}10^{-2}$	$2.75{\cdot}10^{-2}$
$q_{e,onset}$ [kPa]	12.12	21.18	64.88	183.31
$p_{e,onset}$ [kPa]	1.38	3.78	2.62	2.17
$Re^u_{e,onset}$ [m^{-1}]	$5.83{\cdot}10^4$	$7.49{\cdot}10^5$	$3.49{\cdot}10^6$	$5.61{\cdot}10^6$
$c_{p_{e,onset}}$ [-]	0.89	0.48	0.037	0.023
$T_{w,onset} = T_{ra,onset}$ [K]	1,000.0	900.0	1,000.0	1,200.0

W cases, and distinctly larger for the CAV cases. We will discuss the other data of the table in the next sub-section together with the total pressure loss corrected data. In closing this part, we note some guiding principles regarding vehicle-configuration issues. The one-dimensional flow data given in Table 6.2, although being approximate data, represent the optimal onset flow situation. This follows from a simple flow-momentum consideration. The onset flow to an aerodynamic trim or control surface definitely should be as two-dimensional as possible, Sub-Sections 3.2.2 and 4.2.2, and the hinge line of such a surface should be located orthogonally to the onset flow direction. We call this in the following the "optimal onset flow geometry". The trim or control surface itself should have a span, respectively aspect ratio, as large as possible in order to reduce side-edge losses.[7] For the same reason the deflection angles should be as small as possible. The side-edge losses become larger with increasing deflection angle.

We illustrate the matter of onset flow situation with data from a numerical simulation of the flow past the RV-W HOPPER/PHOENIX configuration,

[7] See the considerations in Section 6.6 regarding the influence of flap width and length on the vehicle pitching moment and the hinge moment.

Table 6.3. Flight parameters of the numerical simulation of the flow past the HOPPER configuration [12].

$Case$	M_∞	$Re_{L,\infty}$	L [m]	α [°]	$x/L\|_{trans}$	ε
A	14.4	$8.41{\cdot}10^6$	50.2	31.3	0.5	0.8
B	3.2	$2.31{\cdot}10^7$	50.2	15.0	fully turbulent	0.8

Sub-Section 3.3.6 [12]. The HOPPER configuration was devised and studied in the frame of the "Future European Space Transportation Investigations Programme (FESTIP)" [13], and became later the reference concept of the German national technology programme ASTRA. PHOENIX is the 1:6 downscaled experimental vehicle for low-speed tests in the ASTRA program.

The flight parameters of two trajectory points (cases) are given in Table 6.3. Although in case A the flight Mach number $M_\infty = 14.4$ belongs to a flight altitude above 50 km, it was assumed that laminar–turbulent transition occurs. The transition location was chosen summarily as $x/L = 0.5$. The surface emissivity coefficient was taken to be $\varepsilon = 0.8$.

Figure 6.3 gives the overall view on the lower side of the flight vehicle for case A. All skin-friction lines emanate from the forward stagnation point. The two primary attachment lines lie symmetrically below the forward part of the fuselage and at the wing at a small distance below the leading edge. The skin-friction lines depart (diverge) at these lines to the upper and the lower side of the configuration.[8] At the lower side of the fuselage, which is flat for $x/L > 0.45$, the body flap onset flow is to a good approximation two-dimensional. At the lower side of the wings this is not the case. The wall pressure coefficient varies slightly at the lower side of the configuration, with $c_{p_w} \approx 0.5$ just ahead of the hinge line.

A closer look reveals that the body flap indeed has a nearly optimal onset flow geometry, Fig. 6.4, upper part. It is almost fully two-dimensional and orthogonal to the hinge line. The flow separates at the hinge line due to the extremely large deflection angle $\eta_{bf} = +40°$. Because the onset flow is turbulent, only a small separation regime (relative to the flap length) is present with small upstream influence. The actual distance from the separation line to the attachment line, however, is between ≈ 0.2 m at the symmetry line and ≈ 0.4 m further outboard. Towards the flap edge it becomes distinctly smaller.

Due to the optimal onset flow geometry, we have a nearly constant pressure distribution on a wide part of the flap surface. The pressure rises in downstream direction essentially monotonically towards a plateau value on the flap. The situation on a large part of the body flap resembles case b), Fig. 6.9 in

[8] Compare the flow-field topology with that at the windward side of the Space Shuttle Orbiter, Sub-Section 3.2.2. Obviously, the HOPPER configuration does not have a blunt-cone forebody.

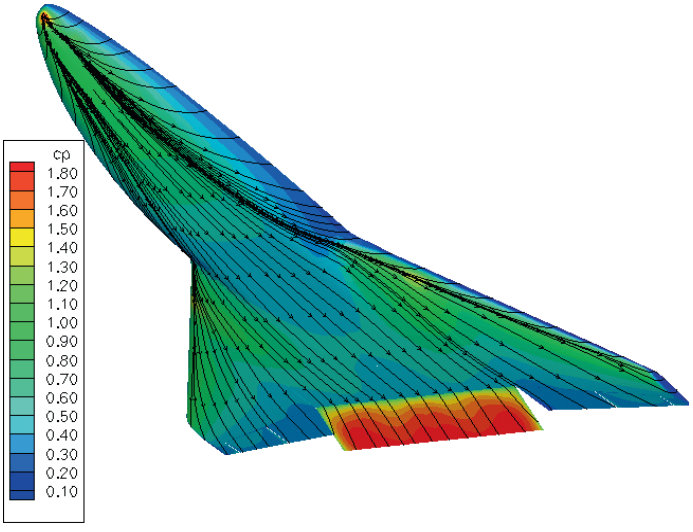

Fig. 6.3. Skin-friction lines and wall pressure coefficient ($c_p \equiv c_{p_w}$) distribution at the lower side of the HOPPER configuration, [12], case A, Table 6.3, downward body flap deflection $\eta_{bf} = +20°$. The body flap has the (chord) length $l_{bf} = 3.5$ m , and the width (span) $w_{bf} = 11.75$ m.

Sub-Section 6.3.1. Near the side edge of the body flap the flow becomes three-dimensional and a pressure relaxation is discernible.

The situation is different for the two wing flaps, Fig. 6.4 lower part, which are multi-functional elevator/aileron surfaces, Sub-Section 6.6.1. The flow situation is clearly sub-optimal. While the flow is only weakly three-dimensional, the hinge lines are strongly swept. The inboard flap which has a small aspect ratio is deflected by $\eta_{iwf} = +20°$. The figure shows a pressure coefficient distribution which is not constant, except for a small part towards the outer edge and the trailing edge. Flow separation at the hinge line, however, is not detectable.

Overall systems demands usually will not permit sweeping configurational changes in order to improve a sub-optimal onset flow geometry. Local changes of the fuselage/wing shape, however, can improve the situation. Given the large flight speed and altitude span of RV-W's and CAV's, an optimization in this sense generally will be very difficult.

6.2.2 Entropy Layer of the Onset Flow

While looking at the literature on flap effectiveness, one can sometimes get the impression that the entropy layer merely leads to additional complications. Hypersonic flight vehicles always have a blunt nose and blunt edges radii because of the thermal loads they have to cope with. A finite radius leads to an entropy

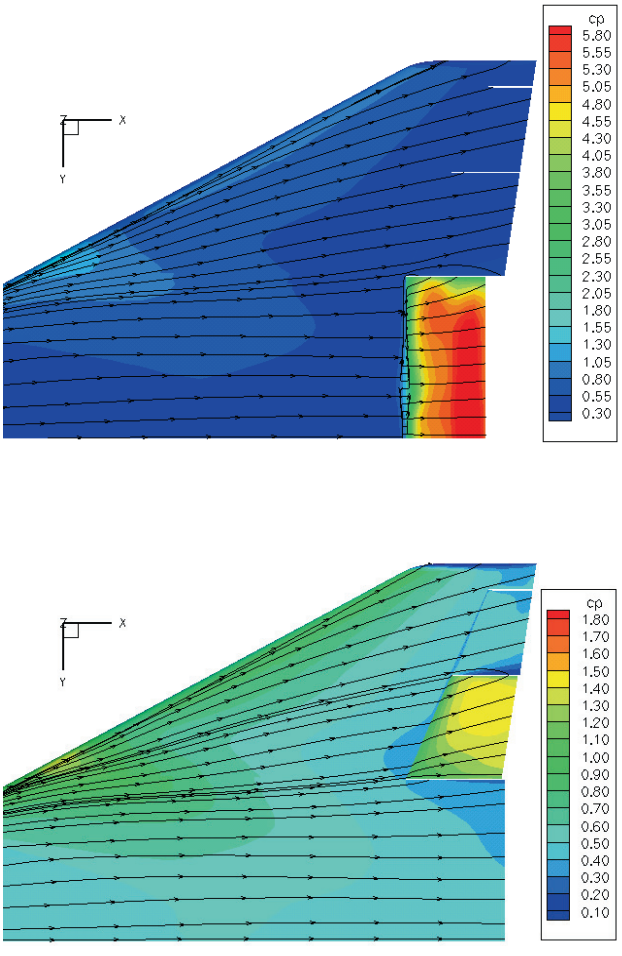

Fig. 6.4. Detailed view of skin-friction lines and wall pressure coefficient ($c_p \equiv c_{p_w}$) distribution at the left lower-side aft part of the HOPPER configuration [12], case A, Table 6.3. Upper part: body flap at $\eta_{bf} = +40°$, lower part: inboard wing flap at $\eta_{iwf} = +20°$. Note that the color coding is different for the two parts.

layer whose thickness depends on the radius, the free-stream Mach number, and high temperature real gas effects.

If the configuration surface downstream of the nose or the leading edge has a large extension in the main flow direction, the entropy layer may be "swallowed" by the developing attached viscous flow, the latter in general being of boundary layer type; i.e., the hypersonic viscous interaction phenomena is weak. For a given blunt-body shape, entropy-layer swallowing is therefore a function of the Reynolds number in the flow regime behind the bow shock. A general discussion of the implications of the entropy layer can be found in [10].

The entropy layer comes into being due to the curvature of a shock surface, here the bow shock surface. In our case the streamline, which crosses the normal-to-the flow portion of the bow shock, experiences the largest entropy rise or total pressure loss. Because the neighboring streamlines have a smaller total pressure loss, the inviscid flow has a velocity gradient in direction normal to the body surface. This is similar to the gradient in a boundary layer, but much weaker, because the inviscid flow does not have a no-slip wall boundary condition. The effect of the entropy layer on the effectiveness of an aerodynamic control surface hence is due to the total pressure loss, which manifests itself mainly in a reduced local dynamic pressure.

Within the simple onset flow consideration, we can approximately take into account the entropy-layer effect by impressing the maximum total pressure loss, i.e., that due to a normal shock, on the one-dimensional inviscid flow, Sub-Section 10.1.5. We use the observation, that with given free-stream conditions the surface pressure depends primarily only on the angle of attack of the considered surface portion (Newton flow property). We keep hence $p_{e,onset}$ from Table 6.2. Proceeding as sketched in Sub-Section 10.1.5, we obtain the onset flow data, corrected by the total pressure loss, given in Table 6.4.

The change of the inviscid onset flow parameters from Table 6.2 to Table 6.4 is dramatic, but different for the two flight vehicle classes, even if this is not yet the final picture, as will be discussed below:

- The reduced total pressure in all cases leads to a distinctly smaller velocity $v_{e,onset,tpl}$. This in turn, with the total enthalpy at the boundary layer edge remaining constant, results in higher temperatures $T_{e,onset,tpl}$ (remember that $Z = 1$ was chosen), and both together in reduced onset flow Mach numbers $M_{e,onset,tpl}$. In the case RV-W 1, the Mach number is now of the order of the actual Mach number at the pressure plateau of the Space Shuttle Orbiter, Sub-Section 3.5.2. While the onset flow Mach numbers of the CAV cases in Table 6.2 indicate that compressibility effects in the turbulent flow must be accounted for,[9] this appears now no more to be the case.
- The reduced velocity $v_{e,onset,tpl}$ causes in concert with the reduced density $\rho_{e,onset,tpl}$ a much reduced dynamic pressure $q_{e,onset,tpl}$ in all cases. The pressure coefficients of course are not changed, they were chosen to be identical: $c_{p_{e,onset,tpl}} \equiv c_{p_{e,onset}}$. The unit Reynolds number $Re^u_{e,onset,tpl}$ is now so small even for CAV's that it could be doubted that the flow is actually turbulent.
- In the case of RV-W 1 we still have a "cold wall" boundary layer situation ($T_{w,onset,tpl} < T_{e,onset,tpl}$), whereas the "hot wall" situation in the other cases has changed to a "cold wall" situation, except for the case CAV 1.

[9] Compressibility effects in attached turbulent flow occur at boundary layer edge Mach numbers $M_e \gtrapprox 5$, Morkovin's hypothesis [8, 14], and must be taken into account in turbulence models.

Table 6.4. Total pressure loss '*tpl*' corrected data (RHPM$^+$ approximation, $Z = 1$) of the lower-side inviscid onset flow of the body flap for the cases RV-W 1, RV-W 2, and elevator/aileron surfaces for the cases CAV 1, CAV 2. The subscript 'e' stands for boundary layer edge condition.

Flight vehicle:	RV-W 1	RV-W 2	CAV 1	CAV 2
M_∞ [–]	20	6	6.8	12
H [km]	70.0	40.0	30.0	34.2
α [°]	40.0	25.0	5.0	5.0
γ_{eff} [–]	1.14	1.4	1.4	1.3
$M_{e,onset,tpl}$ [–]	1.19	1.48	2.81	3.2
$T_{e,onset,tpl}$ [K]	6,954.1	1,428.3	902.1	2,223.8
$v_{e,onset,tpl}$ [m/s]	1,802.0	1,120.2	1,689.2	2,914.8
$\rho_{e,onset,tpl}$ [kg/m^3]	$6.91{\cdot}10^{-4}$	$9.22{\cdot}10^{-3}$	$1.01{\cdot}10^{-2}$	$3.4{\cdot}10^{-3}$
$q_{e,onset,tpl}$ [kPa]	1.12	5.78	14.43	14.45
$p_{e,onset,tpl} \equiv p_{e,onset}$ [kPa]	1.38	3.78	2.62	2.17
$Re^u_{e,onset,tpl}$ [m^{-1}]	$8.53{\cdot}10^3$	$1.98{\cdot}10^5$	$4.42{\cdot}10^5$	$1.42{\cdot}10^5$
$c_{p_{e,onset,tpl}} \equiv c_{p_{e,onset}}$ [–]	0.89	0.48	0.037	0.023
$T_{w,onset,tpl} \equiv T_{ra,onset}$ [K]	1,000.0	900.0	1,000.0	1,200.0

We have noted above that this is not yet the final picture. Why? We have actually considered only the worst picture, viz. the inviscid flow with total pressure loss at the body surface. Actually the inviscid flow away from the surface suffers a smaller total pressure loss than that at the surface, which decreases with increasing distance from the surface and results in the rotational nature of the entropy-layer flow, see, e.g., [10].

However, we must distinguish between two forms of the entropy layer. The first form, typical for symmetric flow, has a velocity profile normal to the body surface like a slip-flow boundary layer. The second form is typical for asymmetric flow, where the streamline hitting the forward stagnation point does not cross the normal-to-the flow portion of the bow shock surface, Fig. 6.5. The computation [15] was made two-dimensionally for the lower centerline of the HALIS configuration [16], see also Sub-Section 3.5.2. In this case, the maximum entropy streamline lies off the body surface and is at the same time the minimum velocity streamline. The entropy layer hence has a wake-like structure. This form possibly is in general present at the windward side of a RV-W configuration at high angle of attack.[10] The profiles of total pressure p_t, pressure p, Mach number M, and velocity v in direction normal to the surface at

[10] In [10], it was sketched, Fig. 6.20, the other way around. Whether we have the second form always on the windward side, cannot be answered.

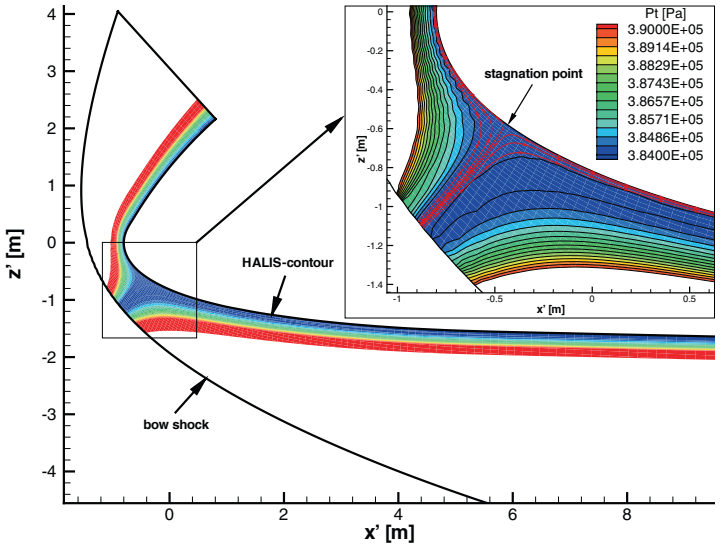

Fig. 6.5. Second form of the entropy layer: computed example, two-dimensional inviscid flow past the centerline of the HALIS configuration, $M_\infty = 10$, $H = 24$ km, $\alpha = 40°$, perfect gas [15]. Total pressure contours and streamlines in the forward stagnation point region.

$x' = 3.99$ m, see Fig. 6.5, are given in Fig. 6.6. The shallow, wake-like structure of the entropy layer off the surface is well discernible.

Whether the second form of the entropy layer is really of influence in our case cannot be decided. Swallowing of the entropy layer by the growing boundary layer,[11] and the accordant change of its edge flow (v_e growing (first form) or first diminishing and than growing (second form)) possibly is of interest mainly for laminar–turbulent transition.

In reality, due to its growing thickness, the attached viscous flow—the boundary layer—swallows the entropy layer partly or even completely, depending on the thickness of the entropy layer and of the boundary layer. The unit Reynolds number and the boundary layer running length are important parameters in this regard, because they govern the boundary layer thickness.

Unfortunately, we cannot illustrate this with our estimated data, but if the entropy layer is swallowed partly or even completely, the external inviscid flow is no more that with the larger total pressure loss, but one with more favorable properties. The dynamic pressure of the onset flow is larger, the edge Mach

[11] This is the usual formulation. A better one would be "the growing of the boundary layer into the entropy layer," which describes the situation better.

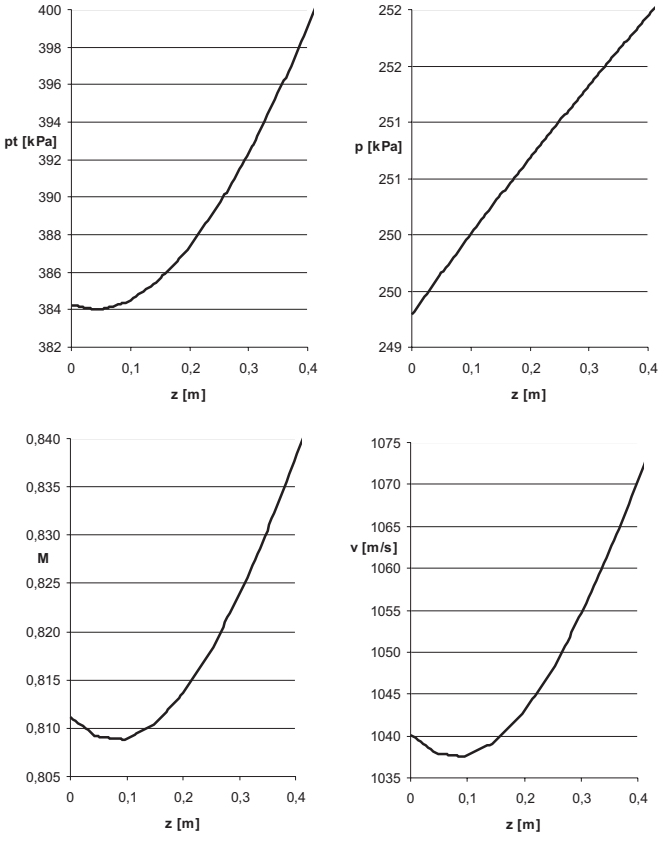

Fig. 6.6. Second form of the entropy layer: computed example, two-dimensional inviscid flow past the centerline of the HALIS configuration, $M_\infty = 10$, $H = 24$ km, $\alpha = 40°$, perfect gas, [15]. Profiles in direction normal to surface at $x' = 3.99$ m, Fig. 6.5: total pressure p_t, pressure p, Mach number M, and velocity v.

number of the attached viscous flow, too, and the attached viscous flow itself is affected.[12]

[12] If we take as phenomenological model of attached viscous flow the boundary layer, we can deduce from its characteristic properties [10], that flow features depend strongly on the local outer (external inviscid flow) and inner (wall) boundary conditions, rather than on the (upstream) initial conditions (however, the local outer conditions are influenced by the swallowed entropy layer). This concerns especially the shapes of the profiles—in direction normal (y) to the surface—of the velocity $v(y)$, the temperature $T(y)$, and the density $\rho(y)$ (via the compatibility conditions). This means, that for the attached viscous onset flow, the locally present external inviscid flow indeed is predominantly of relevance.

The consequence for the onset flow as a whole is, that in any case not the maximum total pressure loss governs the inviscid onset flow, but a smaller one, depending on how much the entropy layer has been swallowed. This is configuration dependent, and different for body flaps, elevators, ailerons and rudders. The boundary layer itself suffers a (strong) total pressure loss, too, which by far compensates the beneficial effects of entropy-layer swallowing. The thickness, and the velocity and density profile shapes (laminar or turbulent flow, thermal state of the surface, see next sub-section) of the attached viscous flow therefore are major factors regarding flap effectiveness, too.

We summarize, concerning the influence of the entropy layer, that the bluntness of a flight vehicle shape influences not only the wave drag and the effectiveness of radiation cooling [10], but also the effectiveness of aerodynamic trim and control surfaces via the onset flow properties.

6.2.3 The Onset Flow Boundary Layer

The properties of the boundary layer, namely, the attached viscous flow part, of the onset flow also influence the effectiveness of an aerodynamic control surface, and especially also the thermal state of the surface and the thermal loads on the flap structure, Sub-Section 6.3.3. To study the first point, we consider the optimal situation of two-dimensional onset flow and a non-swept hinge line.

The two most important properties of the boundary layer are the momentum and its thickness.[13] Both depend strongly on the state of the boundary layer (laminar, transitional or turbulent), and on the local properties of the inviscid flow, with high temperature real gas effects in the background. Of large importance too are the necessary and permissible surface properties, Chapter 9 and [10]. These regard especially transitional and turbulent boundary layers, which react in general strongly on the real-life irregularities of the surface (roughness, steps, gaps, waviness).

A turbulent boundary layer carries more momentum than a laminar one because of the fuller velocity profile $v(y)$, Fig. 6.7, y being the coordinate normal to the surface, provided the density profile $\rho(y)$ is similar in both cases. Therefore, a turbulent boundary layer can negotiate a stronger pressure rise in flow direction without separating. Consequently, the flap angles for incipient separation are far larger for turbulent than for laminar flow.

Another issue is the thickness of the onset flow boundary layer. If the onset flow boundary layer is thin compared to the frontal projection $h_{flap,proj}$ of the deflected control surface, Fig. 6.1, with given length l_{flap} and deflection angle η_{flap}, its influence will be small:

$$\delta_{bl,onset} \ll h_{flap,proj} = l_{flap} \sin \eta_{flap}. \tag{6.2}$$

[13] Depending on the kind of consideration or the employed phenomenological model, the characteristic boundary layer thickness can be the displacement thickness δ_1, the momentum thickness δ_2, or other entities.

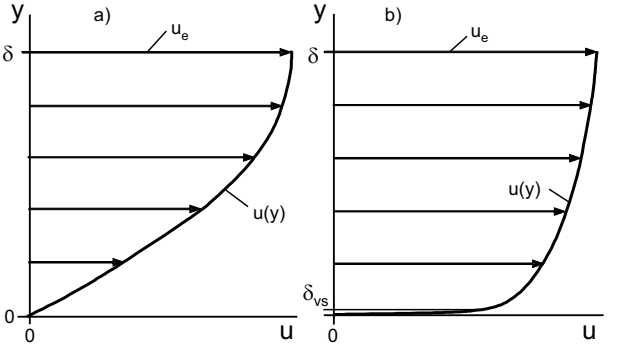

Fig. 6.7. Streamwise velocity profiles of a two-dimensional boundary layer, a) laminar flow, b) turbulent flow [10]. Edge of viscous sub-layer: δ_{vs}.

The deflection angle η^*_{flap}, at which the flap would be fully "buried" in the onset flow boundary layer, is found from:

$$\sin \eta^*_{flap} = \frac{\delta_{bl,onset}}{l_{flap}}. \tag{6.3}$$

In other words, disregarding the state of the boundary layer, laminar or turbulent, the boundary layer thickness will not have much influence on flap effectiveness if $\eta_{flap} \gg \eta^*_{flap}$.

In order to apply the above ideas to the four cases in Table 6.1, we estimate the boundary layer thicknesses of the onset flow at the location of the hinge line for the flow with total pressure correction, Table 6.4. We assume fully laminar flow for the RV-W 1 case, and fully turbulent flow for the cases RV-W 2, CAV 1, and CAV 2. Although the involved temperatures are rather large, we use the reference-temperature approach, Sub-Section 10.4, rather than the reference enthalpy approach. The ensuing errors are acceptable for our illustrating purpose. For the viscosity the simple power-law approximation, eq. (10.61), is employed, which of course becomes unreliable above $T \gtrapprox 1,500$ K. At such temperatures the viscosity is no more a variable of the temperature T only, but, due to high temperature real gas effects, a variable of, for instance, the internal energy and the density [10].

The resulting reference temperatures and unit Reynolds numbers are given in Table 6.5. Compared to the data without total pressure correction—not shown here—the reference temperature is in all cases larger, $T^*_{onset,tpl} > T^*_{onset}$, because $T_{e,onset,tpl} > T_{e,onset}$, and the reference unit Reynolds numbers are changed accordingly. The onset flow boundary layer thicknesses $\delta_{bl,onset,tpl}$ are all larger with total pressure correction, because the Reynolds numbers are smaller.

With the respective flap lengths l_{flap} in Table 6.5, which are estimated data from the reference vehicles, Sub-Section 6.2.1, and the estimated onset flow boundary layer thicknesses $\delta_{bl,onset,tpl}$, we arrive at the η^*_{flap} in the last line. Up

Table 6.5. Onset flow boundary layer thicknesses $\delta_{bl,onset,tpl}$ at the lower vehicle sides of the cases RV-W 1, RV-W 2, CAV 1, and CAV 2, estimated with total pressure loss 'tpl' corrected data from Table 6.4. The second last line gives the (chord) lengths of the body flap, RV-W 1 and RV-W 2, respectively of the elevator/aileron combination (mean lengths), CAV 1 and CAV 2.

Flight vehicle:	RV-W 1	RV-W 2	CAV 1	CAV 2
M_∞ [–]	20	6	6.8	12
H [km]	70.0	40.0	30.0	34.2
α [°]	40.0	25.0	5.0	5.0
γ_{eff} [–]	1.14	1.4	1.4	1.3
l_{onset} [m]	32.0	32.0	25.0	6.0
$T_{w,onset,tpl} \equiv T_{ra,onset}$ [K]	1,000.0	900.0	1,000.0	1,200.0
$T^*_{onset,tpl}$ [K]	4,108.5	1,288.4	1,233.2	2,391.4
$Re^{u*}_{onset,tpl}$ [m^{-1}]	$2.03{\cdot}10^4$	$2.35{\cdot}10^5$	$2.63{\cdot}10^5$	$1.26{\cdot}10^5$
$\delta_{bl,onset,tpl}$ [m]	0.20 (lam)	0.50 (turb)	0.40 (turb)	0.15 (turb)
l_{flap} [m]	2.21	2.21	3.0	0.75
η^*_{flap} [°]	5.2	13.1	7.7	11.5

to these deflection angles the flap is buried in the boundary layer. For turbulent flow these angles are less critical, because of the fuller velocity profile.[14]

Consider case c) of Fig. 6.9. If $\eta_{flap} \lessapprox \eta^*_{flap}$, the interacting shock system, unlike shown in that figure, is buried in the boundary layer. This happens the more, if the flow is turbulent, because in that case the sonic line lies very close to the wall. In any case, of course, the ramp shock of the deflected inviscid flow, the "reattachment shock" in Fig. 6.9, is always there. No systematic studies are available regarding this phenomenon.

We note in passing, that the concave flow situation, which arises when the boundary layer flow enters the deflected flap surface, can lead to a centrifugal instability, with Görtler vortices appearing in the laminar boundary layer, see, e.g., [10]. Such pairwise counter-rotating vortices transport momentum and enthalpy towards the wall. They promote laminar–turbulent transition, enhance thermal loads in the form of streamwise striations, see Sub-Section 6.3.3, and can alter the separation and reattachment behavior of the boundary layer.

We have mentioned above the density profile $\rho(y)$. In this context the above cited "cold" and "hot" wall situation is important. Attached viscous flow is of boundary layer type, if hypersonic viscous interaction and/or low density effects as well as bluntness induced entropy-layer effects, are small or absent.

[14] We do not investigate here, whether the thickness of the viscous sub-layer is the characteristic one in such cases.

If this is true, the pressure in it, in direction normal to the surface, is constant, $p\,(y) = \text{const.}$, at least approximately. This means $\rho_w T_w = \rho(y)T(y) = \rho_e T_e$. Hence for the same inviscid flow a hot wall will result in a small density at and near the wall, and a cold one in a large density. This holds for both laminar and turbulent flow. Since the momentum flux is proportional to the density, the cold-wall situation in general is favorable regarding flap effectiveness. More momentum is transported by the boundary layer flow and the possibility of flow separation is reduced.

The wall temperature, generally the thermal state of the surface, [10], influences not only the density at the wall. As we have seen above, a larger wall temperature also means a thicker boundary layer. It means further also a stronger displacement of the inviscid flow, an enhancement of flow three-dimensionality (the same transverse pressure gradient, but a smaller lateral momentum flux, hence a stronger flow deflection [10]), but, especially for turbulent flow, a reduced wall shear stress, as we will discuss at the end of this sub-section.

Here looms a simulation problem. In flight the vehicle surface is radiation cooled, and therefore we do not have a uniform hot-wall or cold-wall situation. But we definitely have not a cold-wall situation, as we have it in ground-facility simulation. Hence a proper experimental simulation of flap effectiveness can be difficult, if a large accuracy is demanded.

We illustrate the influence of the wall temperature of the onset flow with numerical simulation data again of the flow past the HOPPER configuration [12], Table 6.3, case B. The deflection angle of the body flap is $\eta_{bf} = +20.0°$. We compare two results, upper side in Fig. 6.8: computation with the radiation-adiabatic wall temperature belonging to case B, and lower side: computation with the radiation-adiabatic wall temperature belonging to case A. The wall temperature of the onset flow belonging to case B is about $T_{w,onset,B} = 500$ K (cold case), and that belonging to case A is about $T_{w,onset,A} = 1,500$ K (hot case). On the flap in both cases the temperatures are larger.

We do not contrast here a ground-simulation facility situation with a flight situation. We compare rather a case of possible thermal reversal [10], where the temperature of the TPS surface due to the thermal inertia is still larger than the one which belongs to the momentary flight conditions. However, the situation considered is hardly representative for a real re-entry flight, because in general such a large thermal reversal does not occur.

For both cases we have a nearly optimal onset flow situation. The cold case exhibits a relative small separation region at the hinge line, with small upstream influence, see the discussion of Fig. 6.4. The pressure rises then monotonically towards the well extended pressure plateau on the flap, the situation corresponding on a large part of the flap to case b), Fig. 6.9 in Sub-Section 6.3.1. The three-dimensionality near the edge of the flap is like that which we have seen in Fig. 6.4, where the deflection is two times the present one.

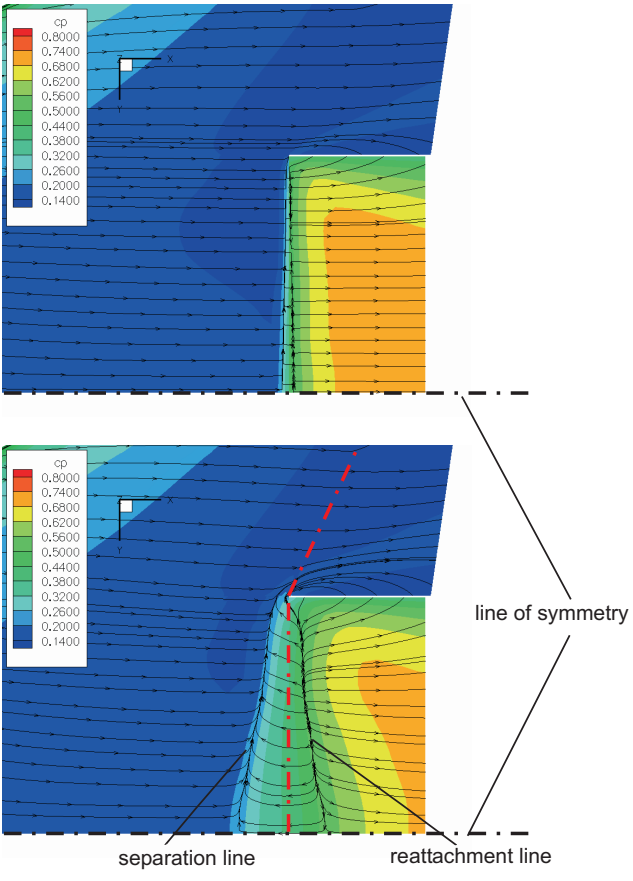

Fig. 6.8. View of skin-friction lines and wall pressure coefficient ($cp \equiv c_{p_w}$) distribution at the left lower-side aft part of the HOPPER configuration, case B, Table 6.3 [12]. Body flap deflection: $\eta_{bf} = +20^\circ$. Upper part: computation results with the radiation-adiabatic wall temperature belonging to case B (cold case), lower part: computation results with the radiation-adiabatic wall temperature belonging to case A (hot case).

The hot case shows some more, but still weak three-dimensionality in the onset flow.[15] Then we see the effect expected due to the low boundary layer momentum: strong separation around the hinge line compared to the cold case. The separated flow regime is characterized by a separation line lying well ahead of

[15] The three-dimensionality ahead of the separation line is caused by a weak transverse pressure gradient of the inviscid flow, and is enhanced by the large wall temperature, see the remark above. The onset flow Mach number ahead of the separation line is around $M_{e,onset} \approx 1.6$, such that the flow is still spatially hyperbolic, and no upstream influence of the deflected flap is present ahead of the primary separation line.

the hinge line (large upstream influence), with the distance largest at the vehicle's symmetry line. The reattachment line lies closer to the hinge line, but has also its largest distance at the symmetry line. The spreading of the distance of the separation and the reattachment line from the cold to the hot case is very similar to that observed in experimental and numerical investigations in two-dimensional (laminar) flat-plate/ramp flow [17, 18]; see also the discussion in [10].

The consequence of the hot case for the flap performance is well discernible. The flap pressure rise seems to be still monotonic, although we should have, at least approximately in the symmetry plane, the pressure overshoot associated with case c), Fig. 6.9, Sub-Section 6.3.1. An extended plateau is not reached, however, the maximum pressure coefficient is like that for the cold-wall case. The flow on the flap surface is highly three-dimensional, the edge effects are stronger. The resulting change in the vehicle pitching moment coefficient from the cold to the hot case is $\Delta C_m = +22.9$ per cent. This is due to the smaller pitch-down flap moment as consequence of the reduced flap force, which counteracts the pitch-up moment of the vehicle, and to the smaller skin-friction on the vehicle's lower side, which has a similar effect. The hinge moment coefficient is changed by only $\Delta C_{m,h} = -4.54$ per cent. It appears to be influenced by the flow around the side edge toward the flap's leeside, where at $M_\infty = 3.2$ the shadow effect anyway is not very strong.

6.3 Asymptotic Consideration of Ramp Flow

6.3.1 Basic Types of Ramp Flow

We consider again the aerodynamic control surface with optimal onset flow geometry. Such flow is classically studied in the form of flat-plate/ramp flow, Fig. 6.1. We assume, that the ranges of onset flow Mach numbers and ramp angles are such that the ramp shocks are only weak shock waves, i. e. in the inviscid case attached shock waves. We begin with looking at the three basic types of flat-plate/ramp flow, shown in Fig. 6.9.

Case a) is the inviscid flow case as it is sketched in Fig. 6.47. We regard its ramp wall-pressure as our asymptotic wall pressure. Case b), shock/boundary layer interaction without separation, is found at small ramp angles and high momentum onset boundary layer flow.[16] It is associated, with a monotonic wall-pressure rise on the ramp towards the plateau pressure (small ramp angles). Finally case c) depicts the flow with significant separation, here sketched with a rather thin onset flow boundary layer. This case, see below, is characterized by a small pressure rise and a pressure plateau upstream of and over the

[16] It appears that a small separation region is always present around the hinge line due to the shock/boundary layer interaction, even for very weak shocks. In the literature sometimes a distinction is made between *true* and *effective* incipient separation.

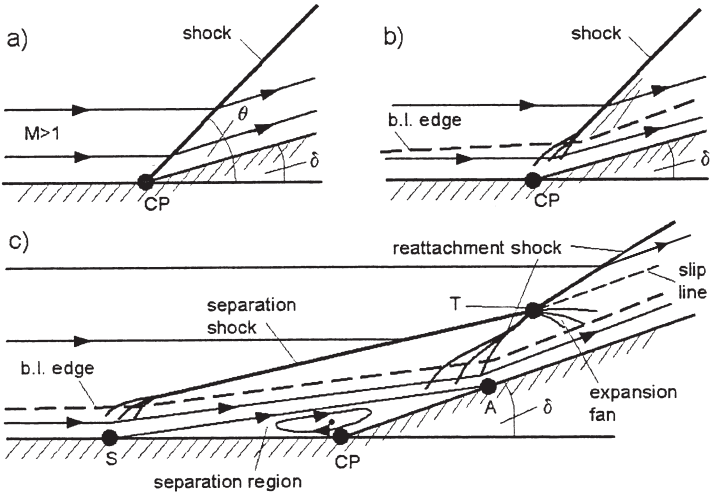

Fig. 6.9. Schematics of two-dimensional flows over a flat-plate/ramp configuration [10]: **a)** inviscid flow, **b)** viscous flow with non-separating boundary layer, **c)** viscous flow with (local) separation; S denotes the separation point, A the reattachment point, T the triple shock point, and CP the corner point.

hinge line and a further monotonic increase of the wall pressure to the ramp plateau. This is typical for small onset flow Mach numbers, or small ramp angles at large onset flow Mach numbers. At large ramp angles or at large onset flow Mach numbers this plateau is approached non-monotonically with a pressure overshoot.

This different behavior is due to the two-shock system (separation shock and reattachment shock in Fig. 6.9, case c), which coalesce in the outer flow to the single ramp shock of case a)). The separation and reattachment shocks have different shock angles and static pressure rise at different combinations of onset flow Mach number and ramp angle. The pressure overshoot just downstream of the reattachment shock becomes stronger with rising onset flow Mach number. With a simple consideration [19], we find for instance for a 14° ramp, that the overshoot appears for $M_1 \gtrapprox 5$, becoming progressively larger with rising M_1.

The available experimental evidence points to the fact that downstream of the pressure overshoot the asymptotic pressure plateau with the pressure of case a) always is approached, provided the ramp is long enough. This happens through the expansion fan emanating at the triple shock point, apart from boundary layer displacement effects. In practice this is in general the case. All three cases occur for laminar as well as turbulent boundary layer flow. Case c) occurs with a laminar onset flow boundary layer at a ramp angle smaller than with a turbulent onset flow.

Criteria for incipient separation, extension of the separation region, and peak heating correlations for laminar, transitional and turbulent flow can be

found in the literature given at the begin of this section. Many of them stem from investigations in cold hypersonic tunnels with cold-wall models. The thickness δ_0 of the onset flow boundary layer at the hinge line (at zero ramp angle), often serving as characteristic length for the separation region upstream of the hinge line, was introduced in [20].

We note here only the criteria for incipient separation. For laminar cold-wall onset flow '1' we have for the incipient separation angle η_{is} [21]; see also [1]:

$$\eta_{is}\,[^\circ] = \frac{80\,\sqrt{\overline{\chi}_1}}{M_1}, \tag{6.4}$$

with the hypersonic viscous interaction parameter for laminar flow

$$\overline{\chi}_1 = \frac{M_1^3\sqrt{C_1}}{\sqrt{Re_{1,l_{onset}}}}, \tag{6.5}$$

and the Chapman–Rubesin constant:

$$C_1 = \frac{\mu_w T_1}{\mu_1 T_w}. \tag{6.6}$$

In [22], experimental data of incipient separation of turbulent flat-plate/ ramp flow were correlated with the inviscid pressure jump belonging to Mach number and ramp-angle pairs. In terms of the pressure jump p_2/p_1 the correlations read

$$M_1 \lessapprox 4.5: \quad \frac{p_{2,is}}{p_1} = 1 + 0.3\,M_1^2, \tag{6.7}$$

and

$$M_1 \gtrapprox 4.5: \quad \frac{p_{2,is}}{p_1} = 0.17\,M_1^{2.5}. \tag{6.8}$$

From these, the incipient-separation ramp angle η_{is}, which belongs to the pressure jump $p_{2,is}/p_1$, can be inferred.

These criteria are of limited value for real flight-vehicle configurations because, besides the actual onset flow geometry, factors like the entropy layer, the wall temperature, the boundary layer thickness, and high temperature real gas effects effectively change the picture. Nevertheless, if the flow situation of the aerodynamic control surface considered meets at least approximately the flow situation, which is the basis of the above and other criteria, assertions can be made.[17]

Here we are interested primarily in the effectiveness of aerodynamic control surfaces. Such surfaces have, in the range of the deflection angles employed, in general an extension of the separation region of only a couple of boundary layer thicknesses δ_0 upstream and downstream of the hinge line. Hence the length of

[17] Detailed discussions of strong interaction flow situations present at real flight vehicle configurations can be found in [5, 7, 23].

Table 6.6. Onset flow parameters of the turbulent flat-plate/ramp flow from [24]. The Reynolds number was found with the thickness $\delta_0 = 0.08$ m of the boundary layer at the hinge line. Test gas is nitrogen.

M_1	T_t [K]	p_t [kPa]	Re_{δ_0}	T_w [K]
9.22	1,070.0	$101,325.0 \cdot 10^3$	$4.0 \cdot 10^5$	295.0

the separation region is much smaller than that of the flap surface l_{flap} itself, Figs. 6.4 and 6.8.

In view of flap effectiveness we hence have in mind the larger part of the flap surface, which is not directly affected by the strong interaction phenomena around the hinge line. We look at the asymptotic behavior of wall pressure, the thermal state of the surface, and the wall shear stress. We assume optimal onset flow. We assume further, that on the ramp surface downstream of the strong interaction domain displacement effects of the boundary layer can be neglected (negligible hypersonic viscous interaction and low-density effects), and that thermo-chemical rate effects are absent. Of course, we develop the asymptotic considerations out of the experimentally observed behavior of the wall entities in the strong interaction domain around the hinge line. In doing this, we make use of the above criteria for incipient separation ramp angles.

6.3.2 Behavior of the Wall Pressure

In Figs. 6.4 and 6.8 we observe on the body flap that apparently the pressure rises monotonically to a peak pressure plateau. We can imagine that this is the pressure of the ideal inviscid ramp flow, Fig. 6.9, case a), and sketched in Fig. 6.47, which we consider as the asymptotically achievable flap pressure. This pressure is a function of the Mach number of the onset flow, the thermo-chemical properties of the gas, and the ramp angle. These in turn are functions of flight speed, altitude and vehicle attitude, Sub-Section 6.1.1.

We turn now to other examples from the literature in order to study the wall-pressure behavior on flat-plate/ramp configurations. First we look at experimental data, Fig. 6.10, which were found with a sharp-edged flat-plate/ramp model [24]. The plate's length from the leading edge to the hinge line was $L = 0.43$ m, the length of the flap was $l_{flap} = 0.1$ m, and its width $w_{flap} = 0.178$ m. The onset flow parameters with a turbulent boundary layer approaching the ramp are given in Table 6.6. We see in Fig. 6.10 that indeed, for all ramp angles, the ideal inviscid ramp pressure is asymptotically reached very fast at only 25.0 to 40.0 mm (four to six hinge-line boundary layer thicknesses δ_0) downstream of the hinge line.

The ramp angle for incipient separation following eq. (6.8) is φ_{is} ($\equiv \eta_{is}$) $\approx 32°$. At the ramp angle $\varphi = 32°$ however, we have already case c), Fig. 6.9, with separation ahead of the hinge line. For $\varphi \leqq 30°$ we have clearly case b)

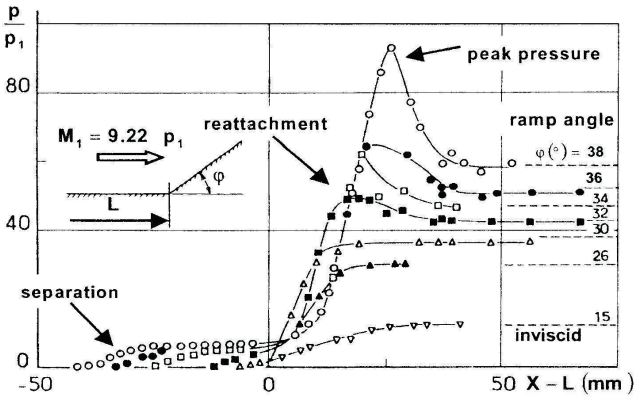

Fig. 6.10. Wall pressure distributions ($p \equiv p_w$) of a turbulent flat-plate/ramp flow as function of the ramp angle φ ($\equiv \eta$) [4], data source: [24]. The onset flow conditions are given in Table 6.6.

with no or only small separation at the hinge line and a monotonic pressure rise just downstream of the hinge line towards the asymptotic value. The upstream influence for $\varphi \geqq 30°$ increases with increasing ramp angle, however, the plateau pressures reached in the separation region ahead of the hinge line are similar. On the ramp, once separation occurs, we see always a prominent overshoot with the peak pressure located in the vicinity (just downstream) of the reattachment point A, Fig. 6.9 c). This is typical for the Edney type IV interaction [25]. The drop of the pressure behind the peak towards the (asymptotic) plateau pressure is due to the expansion starting at the triple point T indicated in Fig. 6.9c).

In the literature, one can find sometimes the summarizing statement, that flow separation reduces flap effectiveness. The pressure distributions shown in Fig. 6.10 for the different ramp angles demand a closer look. Compared to the ideal inviscid wall pressure distribution on the lower side of the flight vehicle and on the flap, sketched in Fig. 6.47, we find that the pressure plateaus indeed do not cover the whole flap surface. This we saw also in Figs. 6.4 and 6.8.

However in Fig. 6.10, we observe two interesting facts concerning the flow on the pressure side of the flap. The first is that if separation is present, the pressure is increased upstream of the hinge line which indirectly enhances the vehicle pitching moment M_{pitch}, Section 6.6. The second is that a monotonic rise of the pressure towards the plateau pressure reduces the hinge moment M_{hinge}. This would happen already if no or only a weak separation is present. But, if an overshoot over the plateau pressure happens, it will partly compensate for the reduced pressure, compared to the ideal inviscid pressure, just downstream of the hinge line.

The balance is delicate; it would be apt to say that viscous effects in any case reduce flap effectiveness, but that separation does not do so in a dramatic

way, unless massive separation is present, as shown, for instance, in Fig. 6.8, lower part. This in general holds also for laminar flow, see the example below. Concerning the hinge moment M_{hinge}, we can say that the monotonic pressure rise reduces it, but that a non-monotonic rise with a pressure overshoot can compensate this to a degree, too. Of course also the length of the control surface compared to that of the affected region (separated flow) around the hinge line must be taken into account.

Before we look at such a flow, we study how present-day numerical simulation methods can cope with turbulent flat-plate/ramp flow.[18] In [26], we find results which are representative for the state of the art regarding the capabilities of Reynolds-averaged Navier–Stokes methods. The onset flow parameters of the selected case, studied experimentally in [27] with the sharp-edged flat-plate/ramp model from [24], are given in Table 6.7.

Table 6.7. Onset flow parameters of the turbulent flat-plate/ramp flow study [26], experimental data from [27]. Test gas is nitrogen.

M_1	p_1 [Pa]	T_1 [K]	Re_1^u [m^{-1}]	T_w [K]	δ_0 [m]
9.22	$2.3{\cdot}10^3$	59.44	$4.7{\cdot}10^7$	295.0	0.008

Figure 6.11 shows the comparison of the experimentally[19] and the numerically found wall pressure distributions for the ramp angle $\eta = 38°$. This would be a rather large flap angle for an aerodynamic control surface. The six applied statistical turbulence models therefore are severely strained. The experimental data are nearly identical with those for the same flap angle shown in Fig. 6.10. No turbulence model reproduces well the pressure rise upstream of the hinge line regarding extent and plateau. On the ramp the asymptotic inviscid pressure plateau is lying at $p_w/p_1 \approx 58.8$. This is reached, with different accuracy, by all turbulence models, but not the magnitude and location of the pressure peak. All in all, given the extremely large ramp angle, the computations are not so bad regarding the wall pressure, although they fail to capture correctly the separation and reattachment process.

Now to the laminar flat-plate/ramp flow: in principle we find the same features as for turbulent flow, but usually exaggerated. This is due to the smaller momentum transported by the onset flow in the laminar boundary layer. In Fig. 6.12, we show measured [28] and computed [17] wall-pressure (above) and Stanton numbers (below) distributions found for a sharp-edged flat-plate/ramp model. The plate's length from the leading edge to the hinge line was $l_{onset} = 0.4389$ m, also the length of the flap was $l_{flap} = 0.4389$ m. The onset flow parameters are given in Table 6.8.

[18] A short discussion of simulation issues is given in Sub-Section 6.7.2.

[19] The work reported in [27] is an extension of that in [24].

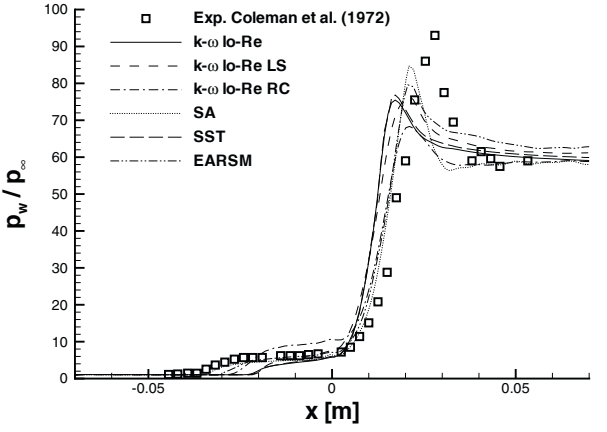

Fig. 6.11. Surface pressure $p_w(x)/p_\infty$ ($\equiv p_w/p_1$) of a turbulent $M_1 = 9.22$ flat-plate/ramp flow with ramp angle $\eta = 38°$, computed with several turbulence models [26] and found experimentally [27]. The onset flow conditions are given in Table 6.7.

Table 6.8. Onset flow parameters of the laminar flat-plate/ramp flow from [17]. Test gas is air.

M_1	T_t [K]	T_1 [K]	Re^u [m^{-1}]	T_w [K]
14.1	3,623.0	88.88	$2.362{\cdot}10^5$	297.22

The non-constant wall pressure ahead of the hinge line (as well as the value $p_w/p_\infty = 1.96$ at $x = 0.395$ m for the lower ramp angle $\theta = 15°$) shows that hypersonic viscous interaction is present. If we take the reference temperature, eq. (10.78), with $T^* \approx 970$ K as a measure, we can speak about a cold-wall situation. With the respective criterion $\overline{\chi}_{crit} \approx 4$ [10], we get hypersonic viscous interaction for $x < x_{crit} \approx 1.9$ m, which seems to confirm this. Nevertheless, we can use the data for the discussion of laminar flat-plate/ramp flow.

The computed wall-pressure data agree sufficiently well[20] with the measured data for both $\theta = 15°$ and $24°$. The criterion eq. (6.4) yields the incipient separation angle $\theta_{is} = 16.3°$. For the $\theta = 15°$ case, indeed, separation is not indicated. The pressure rises monotonically towards the pressure plateau. For the ramp angles larger than $15°$ separation clearly is indicated with growing upstream influence at nearly constant plateau pressure, and the typical overshoot over the ramp plateau pressure behind the hinge line, Fig. 6.12. The asymptotic inviscid plateau pressure is $p_w/p_1 = 24.6$ for the $\theta = 15°$ case and $p_w/p_1 = 58.0$ for the $\theta = 24°$ case. Although hypersonic viscous interaction is present, these values can be considered as a valid approximation of the ramp's plateau pressure.

[20] In [17] grid resolution problems are noted for $\theta > 18°$.

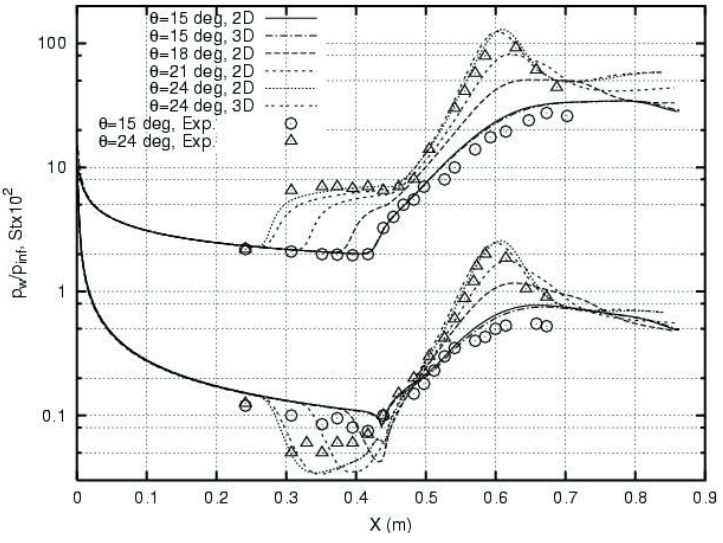

Fig. 6.12. Laminar $M_1 = 14.1$ flat-plate/ramp flow with angles from θ ($\equiv \eta$) = 15° to 24° [17]. The onset flow parameters are given in Table 6.8. Surface pressure $p_w(x)/p_\infty$ ($\equiv p_w(x)/p_1$) (above) and Stanton number $St(x)$ ($\equiv St_{gw}(x)$) (below) were found computationally [17] and experimentally [28].

It remains now to examine the wall-pressure behavior in the presence of laminar–turbulent transition in the vicinity of the hinge line. In [29], for instance, experimental and computational investigations were performed of the flow past a flat-plate/ramp configuration with transition occurring near the reattachment point "A," Fig. 6.9c). The results indicate, regarding the wall pressure distribution, that different assumptions about the state of the boundary layer result in changes around the hinge line, as was to be expected. However, the asymptotic plateau pressure is reached in all cases at a short distance behind the hinge line. Of more concern is the influence of transition on the thermal state of the surface, which is treated in the next sub-section.

Finally, we examine the influence of high temperature real gas effects. Two issues arise here. On the one hand, they may change the inviscid flow geometry (shock angle), the interaction and separation patterns, and the wall pressure around the hinge line. On the other hand, they affect the asymptotic plateau pressure on the flap. Not very much is known about the first issue [4]. Regarding the second issue, we study in a very simple parametric way how the inviscid pressure on the flap p_2 is affected.

For the re-entry type vehicle RV-W 1, Table 6.1, we choose somewhat arbitrarily the onset flow Mach number $M_{e,onset} = 2$, larger than that given in Table 6.4, smaller than that in Table 6.2, in order to take into account entropy-layer swallowing. Otherwise the range of possible ramp-deflection angles with

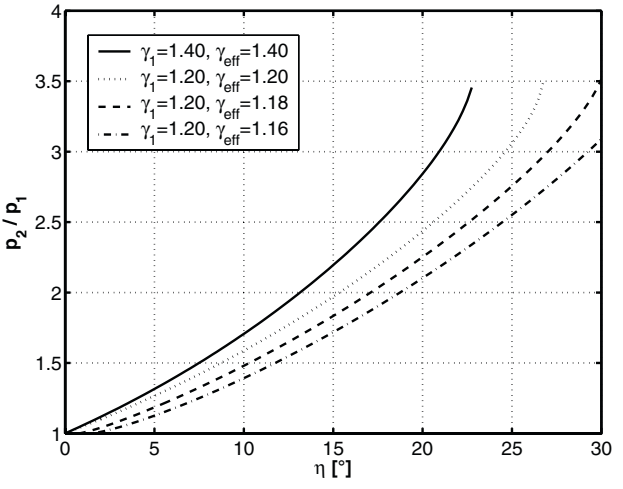

Fig. 6.13. Ratio of ramp pressure to onset flow pressure, p_2/p_1 ($\equiv p_{ramp}/p_{onset}$), as function of the ramp angle η and for $\gamma_1 = 1.2$ and different $\gamma_2 = \gamma_{eff}$. Flight vehicle RV-W 1, Table 6.1, $M_{e,onset} = 2$. If the curves end, this means that the respective ramp shocks become strong shocks and detach.

weak ramp shock would have been too much restricted. The maximum ramp angle was chosen to be $\eta_{ramp} = 30°$, Figs. 6.13 and 6.14.

High temperature real gas effects were simulated by choosing different ratios of effective specific heats. The influence of the ratio of specific heats in the onset flow ahead of the ramp was studied with $\gamma_1 = 1.2$ in Fig. 6.13 and $\gamma_1 = 1.16$ in Fig. 6.14. Accordingly, smaller values of $\gamma_2 = \gamma_{eff}$ were chosen for the flow on the ramp.

What we see in Fig. 6.13 for a given ramp angle η is a decrease of the asymptotic plateau pressure p_2 with decreasing γ_{eff}, i.e., increasing high temperature real gas effects. The pressure span for, say, $\eta = 20°$ is moderate with $p_{ramp}/p_{onset} \approx 2$–$2.8$ for the range of γ_{eff} considered. The percentage of the influence of γ_{eff} is rather large. With $\gamma_{eff} \approx 1.14$ reflecting reality, a simulation of the flow with, for instance, perfect gas, i.e. $\gamma = 1.4$ would lead to unrealistic large flap effectiveness.[21] The effects are somewhat increased for the smaller γ_1, Fig. 6.13

We note also in Figs. 6.13 and Fig. 6.14, that the pressure ratio increases faster with increasing ramp angle. We can show this explicitly for large Mach numbers and small ramp angles. With [10]

$$M_1 \to \infty,\ \eta \text{ small}: \ c_{p_2} \to \frac{4sin^2\theta}{\gamma+1},\ \theta \to \frac{\gamma+1}{2}\eta \tag{6.9}$$

[21] The decreasing γ_{eff} has another effect. It shifts the ramp angle at which the oblique shock detaches to form a strong shock to significantly larger values.

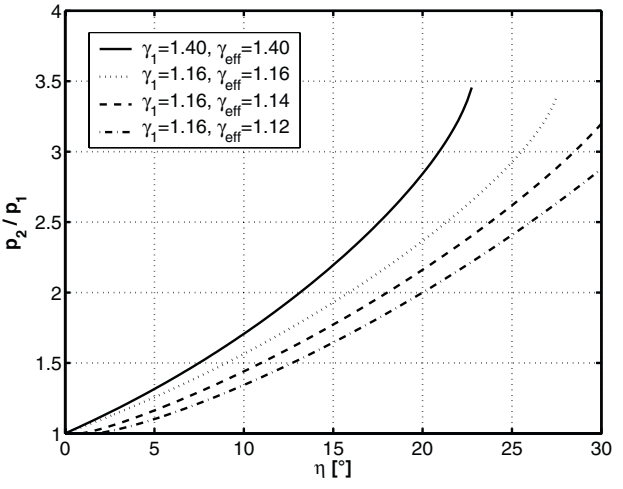

Fig. 6.14. Ratio of ramp pressure to onset flow pressure, p_2/p_1 ($\equiv p_{ramp}/p_{onset}$), as function of the ramp angle η and for $\gamma_1 = 1.16$ and different $\gamma_2 = \gamma_{eff}$. Flight vehicle RV-W 1, Table 6.1, $M_{e,onset} = 2$. If the curves end, this means that the respective ramp shocks become strong shocks and detach.

we find, locally applied, assuming constant γ, with the Mach number retained due to the definition of c_p:

$$\begin{aligned} M_1 \to \infty,\ \eta \text{ small} : \Delta\left(\frac{p_2}{p_1}\right) = \frac{p_2 - p_1}{p_1} \to \frac{\gamma(\gamma+1)}{2} M_1^2 \eta^2, \\ \Rightarrow \Delta\left(\frac{p_2}{p_1}\right) \sim \eta^2, \frac{d}{d\eta}\left[\Delta\left(\frac{p_2}{p_1}\right)\right] \sim \eta. \end{aligned} \tag{6.10}$$

The increase of a flap's pressure ratio with η^2 and of the gradient with η for supersonic flow is reflected directly by any related moment and its gradient; see [30] and also below.

The γ_{eff} effect found in Figs. 6.13 and Fig. 6.14, however, must be considered carefully. The reality is much more complex. Assume a RV-W in the RHMP$^+$ approximation for a given speed, altitude and angle of attack. If we model the flow past it with different high temperature real gas approximations in terms of γ_{eff}, we observe that for any $\gamma_{eff} > \gamma_{eff,nominal}$ that the temperature of the flow at the windward side of the vehicle is larger than that belonging to $\gamma_{eff,nominal}$. Because onset flow pressure and velocity are not much affected, the onset flow Mach number would be smaller in these cases than for $\gamma_{eff,nominal}$, which certainly would change the results.

We study this with an example available in the literature. The flow past the Space Shuttle Orbiter was investigated with a Navier–Stokes code for the flight situation and the tunnel situation [31]. Table 6.9 shows the flight parameters of the two computation cases. We look first at the wall pressure ratio

Table 6.9. Parameters of the computational study of the flow past the Orbiter for the flight (STS-1) and the tunnel situation [31]. Laminar flow with no-slip boundary conditions was assumed, the flight situation was computed with a non-equilibrium real-gas model and a catalytic wall condition.

Computation case	M_∞ [-]	Altitude [km]	$L_{vehicle}$ [m]	v_∞ [km/s]	ρ_∞ [kg/m^3]	T_∞ [K]	T_{wall} [K]
Flight situation	23.68	73.1	32.77	6.81	$5.29{\cdot}10^{-5}$	205.0	rad.-adiab.
Tunnel situation	10	-	0.246	1.42	$788.0{\cdot}10^{-5}$	50.0	ambient

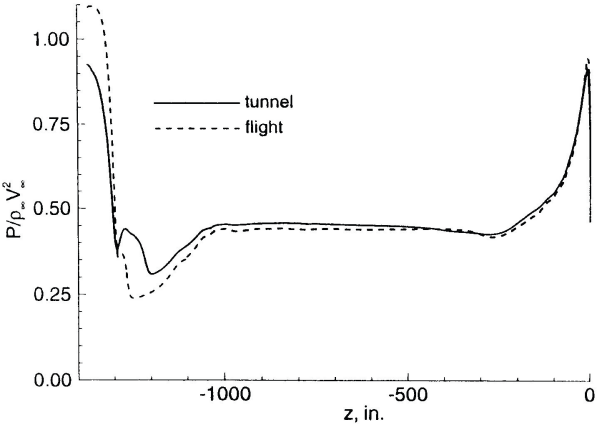

Fig. 6.15. Wall pressure distributions at the lower symmetry line of the Space Shuttle Orbiter at $\alpha = 40^\circ$, body flap deflection $\eta_{bf} = 20^\circ$ [31]. The broken line gives the pressure distribution in the flight situation, the full line that of a perfect-gas tunnel situation. The forward stagnation point is at the right, the body flap at the left.

at the lower symmetry line of the Space Shuttle Orbiter. Fig. 6.15, [31], shows that in the flight situation the dimensionless pressure on the body flap (at the far left in the figure) is larger than in the tunnel situation (perfect gas). This is opposite to the result, which we see in Fig. 6.13. The cause is the change of the onset flow Mach number due to real-gas effects. This Mach number is larger in the flight situation. The real-gas effects hence dominate the pressure ratio indirectly more via the onset flow Mach number than directly, as shown in Fig. 6.13.

This is illustrated in Table 6.10, where ramp-shock angles $\theta_{ramp\ shock}$ and pressure ratios p_{ramp}/p_{onset} are given. They were obtained with the M_{onset} and γ_{eff} data determined in [31] from the computations.[22] The present data

[22] Keeping in mind the influence of entropy-layer swallowing on the onset flow Mach number, its exact determination from a Navier–Stokes computation is somewhat problematic, because there the boundary layer edge is not clearly

Table 6.10. Ramp-shock angles $\theta_{ramp\ shock}$ and pressure ratios p_{ramp}/p_{onset} of the laminar flat-plate/ramp flow for $\eta_{bf} = 20°$ obtained with onset flow parameters M_{onset}, γ_{eff} [31].

Computation case	M_{onset}	γ_{eff}	$\theta_{ramp\ shock}$	p_{ramp}/p_{onset}
Tunnel situation	2.13	1.4	49.60°	2.90
Flight situation	3.45	1.2	32.75°	3.71

are in fair agreement with the pressure rise on the body flap shown in Fig. 6.15 for both cases[23], and show in any case that indeed the onset flow Mach number is of large importance. The most important result from [31] regarding flap effectiveness and real-gas effects in view of the whole vehicle, the Space Shuttle Orbiter, is shown in Fig. 6.16. Plotted is the incremental pitching moment $\Delta C_m = C_{m,\eta_{bf}} - C_{m,\eta_{bf=0}}$ as a function of the body flap deflection angle η_{bf} and the angle of attack α. The results, again for the flight situation and for the perfect-gas tunnel situation, like in Fig. 6.15, show the influence of presumably the high temperature real gas effects on the pitching moment of the flight vehicle. Their influence implicitly increases for increasing angle of attack (body flap onset flow characteristics), and for increasing body flap angle. For $\alpha = 40°$ and $\eta_{bf} = 20°$ the body flap effectiveness is almost 50 per cent larger if real-gas effects are regarded. Also the (negative) gradient of the moment with regard to the deflection angle, $C_{m,\eta} = dC_m/d\eta$, increases with η_{bf}, see above, eq. (6.10), and that stronger for the flight case than for the wind tunnel case.

The authors of [31] discuss their results with all caution. The influence of the slight geometrical changes of the vehicle shape for the computations, of the aeroelastic deformation of the body flap, elevon gap flow, base pressure, leeside pressure on the body flap, and viscous effects is considered. The free-stream Reynolds numbers are $O(10^6)$ in both cases. The actual onset flow Reynolds numbers are not given. All in all, it appears that high temperature real gas effects, via the change of the onset flow Mach number, are the major cause of the discrepancies between flight and wind-tunnel data.

The basic conclusion is that the body flap of the Space Shuttle Orbiter is more effective in flight than was determined in perfect gas, ground facility simulation. The hypersonic pitching moment anomaly, which was observed on STS-1, Section 3.5, thus appears not to be caused by reduced flap effectiveness in flight, as is sometimes asserted in the literature. On the contrary, ... *had the*

indicated. We note further, that obviously the boattailing has a positive effect regarding the effectiveness of the body flap, because it increases the onset flow Mach number. This effect holds also for the elevators/ailerons at the wing's trailing edge, Fig. 6.44.

[23] The data given in [31] are significantly smaller, because the ramp-shock angles employed there are smaller.

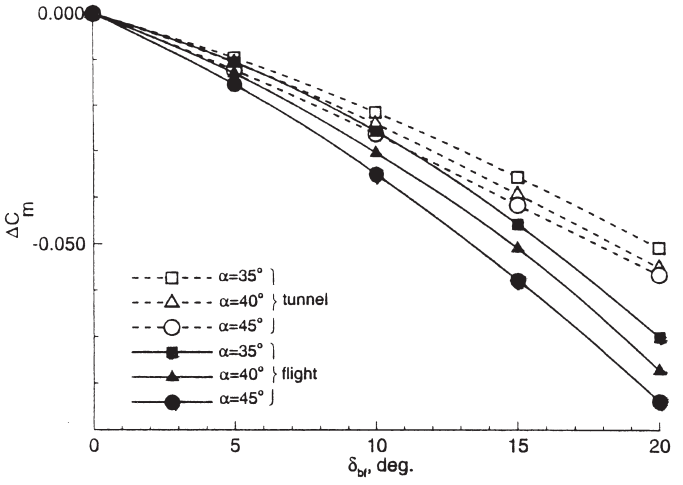

Fig. 6.16. Computed incremental pitching moment $\Delta C_m = C_{m,\eta_{bf}} - C_{m,\eta_{bf}=0}$ of the Orbiter as function of the body flap deflection angle δ_{bf} ($\equiv \eta_{bf}$) and the angle of attack α, [31]. The full lines gives ΔC_m in the flight situation, the broken line that of the perfect-gas tunnel situation.

body flap exhibited the same effectiveness in flight as in the tunnel, the vehicle may not have (been) trimmed at all [31].

Back to Fig. 6.13, we have seen there that for RV-W's at large angle of attack the (asymptotic inviscid) pressure rise on the flap as function of the deflection angle is not large because then the onset flow Mach number is small. Moreover, the influence of the parameter γ_{eff} is moderate. We have also learned that onset flow Mach numbers themselves depend on high temperature real gas effects and that this must be taken into account because it can be the deciding factor regarding flap effectiveness.

On CAV's, the onset flow Mach numbers are large and the picture changes. We show this in Fig. 6.17 where, for the hypersonic aircraft type vehicle CAV 2, Table 6.1, the pressure rise is given as function of η_{ramp} and three different γ_{eff}. Again we have chosen somewhat arbitrarily an onset flow Mach number, now $M_{e,onset} = 10$, larger than that given in Table 6.4 but smaller than that in Table 6.2, in order to take into account entropy-layer swallowing.

We see a behavior qualitatively like that in Fig. 6.13. The pressure span for $\eta_{ramp} = 20°$ however is now much larger with $p_{ramp}/p_{onset} \approx 20$ to 22 for the range of γ_{eff} considered. The percentage of the γ_{eff} effect is a lot smaller. Also here an indirect influence of high temperature real gas effects via the onset flow Mach number exists. Even if it is smaller than in the case of RV-W's, it must be regarded in the vehicle design.

These exercises have shown in an approximate way the basic influence of high temperature real gas effects (indirectly also via the onset flow Mach number) on the effectiveness, in terms of the asymptotic plateau pressure due to

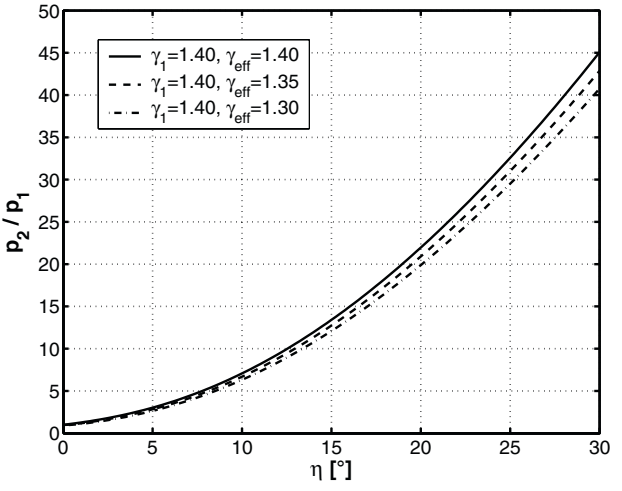

Fig. 6.17. Ratio of ramp pressure to onset flow pressure, p_2/p_1 ($\equiv p_{ramp}/p_{onset}$), as function of the ramp angle η and three different γ_{eff}. Flight vehicle CAV 2, Tables 6.1 and 6.2, $M_{e,onset} = 10$.

a weak shock wave, of an aerodynamic trim or control surface with optimal onset flow geometry. In reality, a more thorough investigation such as [31] is necessary in order to get the influence of all relevant parameters right. Special problems arise if a sub-optimal onset flow geometry is given, for instance at elevators, ailerons, and rudders. Of course also the wider problem of stabilization surfaces, for instance vertical stabilizers, needs special attention.

6.3.3 Behavior of the Thermal State of the Surface

The asymptotic thermal state of the surface on an aerodynamic trim or control surface can be constructed at least approximately, if we consider the flat-plate/ramp configuration with optimal onset flow geometry. As we have already seen, the pressure on the ramp asymptotically reaches a plateau. Regarding, for instance, the heat flux in the gas at the wall, q_{gw}, we can imagine that its distribution on the ramp asymptotically is somehow proportional to the inverse of the boundary layer thickness for laminar flow, or to the inverse of the thickness of the viscous sub-layer for turbulent flow, and hence to the inverse power of the boundary layer running length x. This is sketched in Chapter 9 [10]. The radiation-adiabatic temperature will behave accordingly.

The large increase of both the heat flux in the gas at the wall and the radiation-adiabatic temperature on the ramp, compared to those on the flat plate, is mainly due to the decrease of the boundary layer thicknesses. These depend, in different ways, inversely on the local unit Reynolds number $Re_e^u = \rho_e v_e/\mu_e$, Sub-Section 10.4.2, hence $q_{gw} \sim (Re_e^u)^{1-n}$ and $T_{ra} \sim (Re_e^u)^{0.25(1-n)}$;

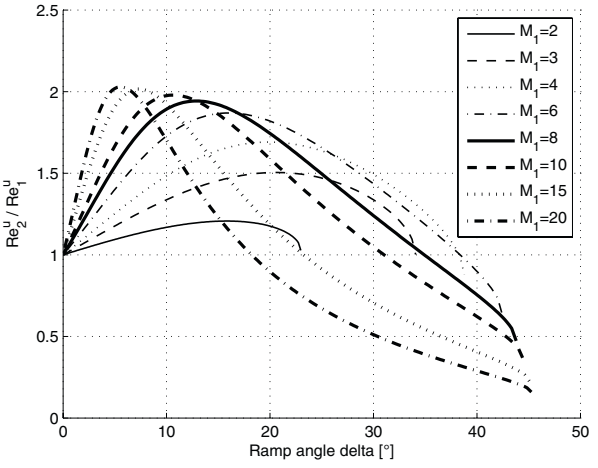

Fig. 6.18. Ratio of unit Reynolds numbers across the shock of a flat-plate('1')/ ramp('2') configuration as function of the ramp angle η for different flat-plate Mach numbers M_1 and the ratio of the specific heats $\gamma = 1.4$ [32]. The viscosity μ in all cases was computed with the power-law relation, eq. (10.61), hence the figure holds for temperatures $T_1, T_2 \gtrapprox 200$ K.

$n = 0.5$ for laminar and $n = 0.2$ for turbulent flow, Sub-Section 10.4.3. Intuitively one would assume that Re_e^u rises always across the shock wave of a flat-plate/ramp configuration. In [10], it is shown and explained that this is not true. We illustrate this in Fig. 6.18.

Take for instance the Mach number $M_1 = 8$. For $0° < \eta < 35°$ we have $Re_{e,2}^u > Re_{e,1}^u$, with a maximum around $\eta \approx 12°$. This means that in this interval, all boundary layer thicknesses on the ramp ('2') will be smaller than those on the flat plate ('1'). For $\eta > 35°$, the opposite is true. For smaller Mach numbers M_1, smaller maximum ramp angles with weaker shocks are reached, the ratios and their maxima become smaller, too. Interesting is that for larger Mach numbers the ramp angles decrease, for which the unit Reynolds number ratios become < 1. Then also the maxima are more pronounced, lying around two. High temperature real gas effects in general increase the maxima of the unit Reynolds number ratios and shift the ratios smaller than one to larger ramp angles.

Unfortunately, this does not influence the thermal state of the surface in the same way. Both the heat flux in the gas at the wall and the radiation-adiabatic temperature increase always with increasing ramp angle, because of the increase of the temperature, $T_{e,2} > T_{e,1}$, and hence of the thermal conductivity $k_{e,2}$ and of the reference temperature T^*, Sub-Section 10.4.3. Nevertheless, the particular behavior of the boundary layer thicknesses, as well as of the thermal state of the wall, and of the shear stress with $\tau_w \sim (Re_e^u)^{1-n}$, can be of interest

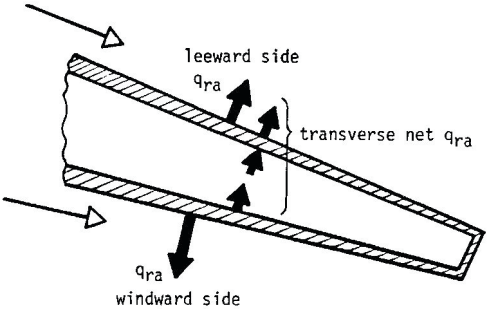

Fig. 6.19. Transverse heat transfer, by either thermal radiation q_{ra} or heat conduction q_w through a flap structure for cooling purposes [33].

in view of several flow phenomena. Depending on M_1 and γ_{eff} one can choose the ramp angle either to make use or to avoid the peak value of Re_2^u/Re_1^u.[24]

Prerequisite for the above postulated asymptotic behavior of the heat flux in the gas at the wall is a constant wall temperature, or a constant (small) heat flux into the wall (in the presence of surface radiation cooling). This means, for instance, negligible transverse heat conduction/radiation through the structure of the flap, Fig. 6.19, and negligible non-convex effects, i. e. no mutual radiative heat exchange between surface portions, Section 9.1.

We now analyze experimental flat-plate/ramp wall heat transfer data. For laminar flow these are given in Fig. 6.12 in terms of the Stanton number St, and for turbulent flow in Fig. 6.22 in terms of the normalized heat flux in the gas at the wall q_{gw}/q_{ref}. Our analysis makes use of the reference-temperature relations given in Sub-Section 10.4.3 for the heat flux in the gas at the wall at flat surfaces (these relations indeed show the above mentioned asymptotic behavior). The employed pressure is the constant inviscid pressure on both the flat plate and on the ramp. On the latter this is the asymptotic plateau pressure downstream of the oblique shock wave. The relations for the determination of the virtual origin of the ramp boundary layer for the flat-plate/ramp configuration are provided in Sub-Section 10.4.4.

The application to the experimental 15° flat-plate/ramp data in Fig. 6.12, which is the case without separation, yields the result shown in Fig. 6.20. We observe, although we have only few experimental data points of the Stanton number, that they follow the $x^{-0.5}$ proportionality ahead of the hinge line as well as asymptotically on the flap, Sub-Section 10.4.3. The increase around the hinge line is monotonic. The agreement between the experimental and the reference-temperature data appears to be as good as that between the Navier–Stokes data and the experimental data in Fig. 6.12. However, we must keep in mind that hypersonic viscous interaction is present.

[24] We observe for the skin-friction coefficient $c_f \sim (Re_e^u)^{-n}$, Sub-Section 10.4.3.

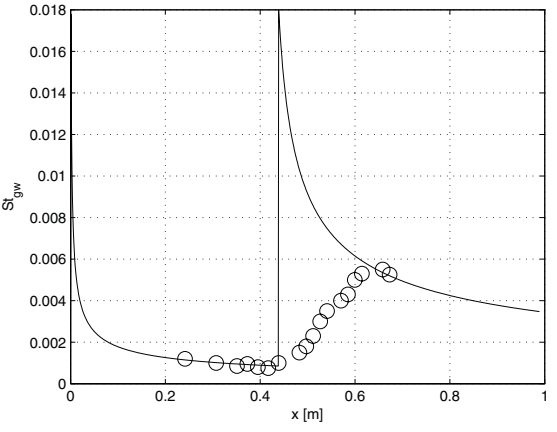

Fig. 6.20. Laminar $M_1 = 14.1$ flat-plate/ramp flow with θ ($\equiv \eta$) $= 15^\circ$ [17], see Fig. 6.12. Asymptotic behavior of the Stanton number $St_{gw} = q_{gw}/[\rho_\infty v_\infty (h_t - h_w)]$ as function of the location x, Fig. 6.12. The circles represent the experimental data [28], the line the data found with the reference-temperature approach.

For the 24° flat-plate/ramp data in Fig. 6.21, the case with separation, the picture is not so good. Again, we do not have enough experimental data on the ramp. Ahead of the hinge line, we see the expected $x^{-0.5}$ behavior of the Stanton number, followed by a steep rise towards a maximum which lies in the vicinity of the reattachment point A, Fig. 6.9c), where the characteristic boundary layer thickness has a minimum. Downstream of that, the Stanton number tends towards towards the $x^{-0.5}$ behavior, however, without fully reaching it.

Data in terms of the normalized heat flux in the gas at the wall q_{gw}/q_{ref} for turbulent flow past a 38° flat-plate/ramp configuration are given in Fig. 6.22. They belong to the pressure data shown in Fig. 6.11. Other than for the pressure, the agreement between the computed [26] and the measured [27] data is not good. The large boundary layer edge Mach number leads to large compressibility effects which, together with the strong compression at the ramp, show up stronger in the heat flux in the gas at the wall, than in the wall pressure.

All turbulence models predict the rise of the heat flux on the flat plate too close to the hinge line, i.e., they underpredict the extent of separation. The experimentally observed rise lies at $x \approx -0.055$ m. The following increase of the heat flux downstream of the hinge line is predicted too early and too steep, with a peak too high, by all employed turbulence models, except for the k–ω low Reynolds number model with rapid compression (RC) correction (k–ω lo-Re RC). This model still gives a rise that is too steep but a peak lower than the experimental one.

The application of the reference-temperature relations, with the junction treated as in the laminar cases above, to the case in Fig. 6.22 gives, due to the chosen reference heat flux, a constant ratio equal to unity ahead of the

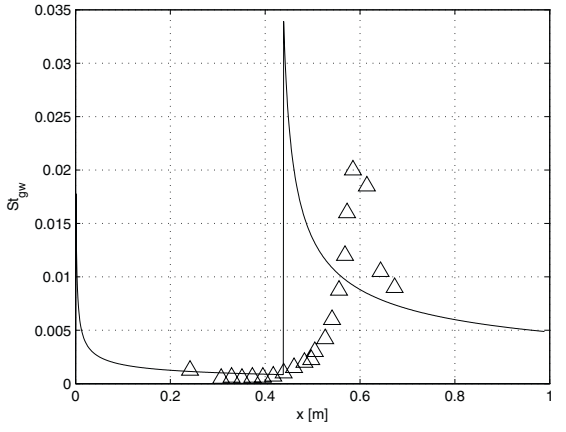

Fig. 6.21. Laminar $M_1 = 14.1$ flat-plate/ramp flow with $\theta \ (\equiv \eta) = 24^\circ$ [17], see Fig. 6.12. Asymptotic behavior of the Stanton number St_{gw} as function of the location x, Fig. 6.12. The triangles represent the experimental data [28], the line the data found with the reference-temperature approach.

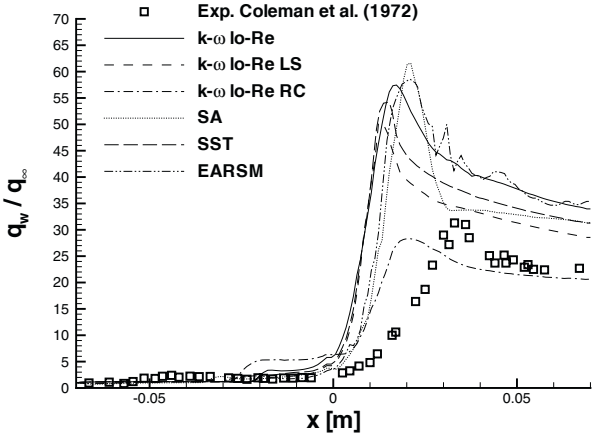

Fig. 6.22. Non-dimensionalized heat transfer in the gas at the wall $q_w(x) \ (\equiv q_{gw}(x))$ for turbulent $M_1 = 9.22$ flat-plate/ramp flow with $\eta = 38^\circ$ [26], see also Fig. 6.11. Computed data obtained with several turbulence models and experimental data [27]. The reference data $q_{ref} = q_\infty \equiv q_{gw,ref}(x)$ are found in the entire x-interval for the ramp angle $\eta = 0^\circ$.

hinge line, Fig. 6.23. On the ramp in the vicinity of the reattachment point A at $x \approx 0.04$ m, Fig. 6.9 c), the experimental heat-flux data begin to tend toward the asymptotic $x^{-0.2}$ behavior typical for turbulent flow. Results can be improved by using the approximate procedure proposed in [34], see, e.g., also [29], to put the virtual origin of the ramp boundary layer in the vicinity of the reattachment point on the ramp. That gives a quite good correlation of

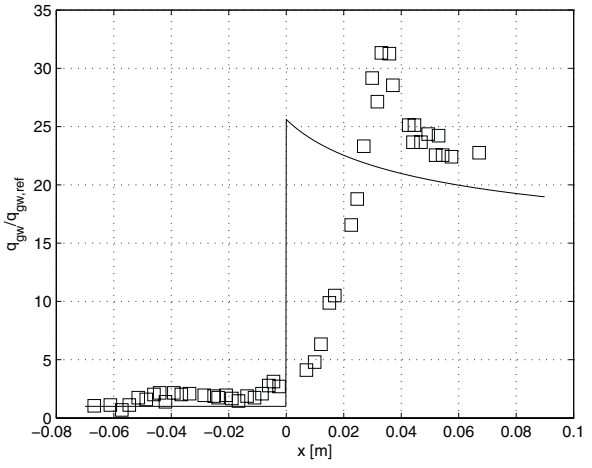

Fig. 6.23. Turbulent $M_1 = 9.22$ flat-plate/ramp flow with $\eta = 38^\circ$ [26]. Asymptotic behavior of the non-dimensionalized heat transfer in the gas at the wall $q_{gw}(x)$ as function of the location x, Fig. 6.22. The reference data $q_{gw,ref}(x)$ again are found in the whole x-interval with $\eta = 0^\circ$. The squares represent the experimental data [27]; the line represents data obtained with the reference-temperature approach.

the experimental data, nevertheless, in contains a certain ambiguity, therefore we do not show such results.

The behavior of the data in Fig. 6.23, also that of the data with the procedure of [34, 29], is possibly a sign that, very shortly downstream of the reattachment point, that the viscous sub-layer is fully reestablished, again an indication that boundary-layer like flow depends stronger on the boundary conditions than on the initial conditions.[25]

Although the k–ω lo-Re RC turbulence model in Fig. 6.22 meets the level of the experimental data, it appears not to show fully the proper asymptotic behavior which the other models seem to do, with the exception of the Spalart–Allmaras model (SA). Whether and how these establish the level of the experimental data further downstream is not known. In any case, all but one turbulence model would predict thermal loads too large not only in the strong interaction region, but probably also on the remaining flap surface.

The test case is very demanding. Turbulence/compressibility effects play a role but also the large pressure rise and the complex interacting flow field. The conclusion in [26] about the performance of the turbulence models—fair to good prediction of the pressure, see above, generally not so good for the heat flux—therefore cannot be generalized. In general, it holds that the performance of turbulence models in strongly interacting flows, particularly with

[25] This seems to contradict the observation of D.C. Wilcox, [14], that the local state of a turbulent flow depends on the upstream history and therefore cannot be uniquely specified in terms of the local strain-rate tensor as in laminar flow.

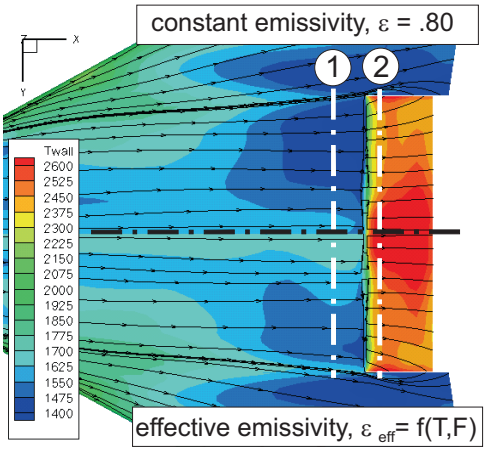

Fig. 6.24. Distribution of the radiation-adiabatic temperature T_{ra} ($\equiv T_{wall}$) and the skin-friction lines at the lower-side aft part of the HOPPER configuration, case A, Table 6.3 [12]. Body flap deflection: $\eta_{bf} = +40°$. Upper part: computed distribution with constant emissivity coefficient $\varepsilon = 0.8$. Lower part: computed distribution with effective emissivity ε_{eff}, taking into account non-convex effects; F is the geometrical factor which quantifies the non-convexity.

flow separation, in the high-speed as well as in the low-speed domain, for the latter, see, e.g., [35], still need significant improvement.

Regarding the asymptotic behavior of the radiation-adiabatic temperature on the ramp for either laminar or turbulent flow, no data are available to analyze. Ground facility simulation of this temperature is not possible [10] and suitable flight data are not available. Following eq. (10.101) it is, however, permitted to assume a $x^{-0.25n}$ behavior.

In this context, non-convex phenomena, related to surface-radiation cooling, need to be considered. At a control surface, their influence increases with increasing angle of deflection.[26] Figures 6.24 and 6.25 [12] show results concerning these phenomena in the vicinity of the body flap of the HOPPER configuration, case A in Table 6.3, $\eta_{bf} = +40°$. In the upper part of Fig. 6.24 the computed radiation-adiabatic wall temperature distribution with constant emissivity coefficient $\varepsilon = 0.8$ is given, in the lower part that computed with the effective, or fictitious, emissivity coefficient ε_{eff}, taking into account, using the GETHRA code in the form derived in [36], non-convex effects due to the deflected flap.

[26] We concentrate the following discussion on the primary problem which occurs with radiation cooling of the onset flow surface of the flight vehicle and of the flap surface. The problem of non-convex effects in the flap gaps or, like in the case of the X-38, on the back side of the split body flap/elevon in the fuselage cavity, needs special attention, see below.

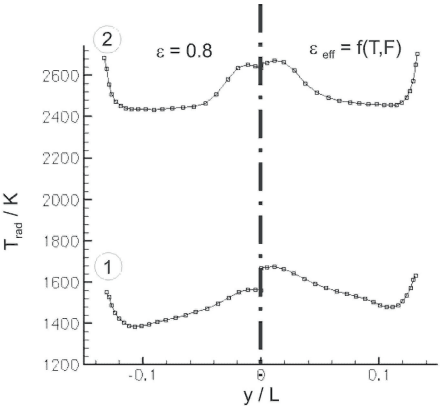

Fig. 6.25. Details of the solutions shown in Fig. 6.24 [12]: spanwise temperature distributions at position 1 in the onset flow regime, and at position 2 on the body flap, left side with constant emissivity, right side with non-convex effects, Figs. 6.24.

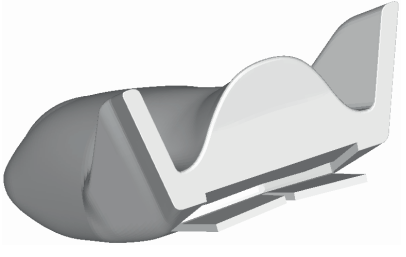

Fig. 6.26. Backside of the X-38 with the cavity above the split body flap/elevon, $\eta_{bf} = +20°$ [37].

On the lower side of the flight vehicle, the radiation-adiabatic temperature decreases in both cases towards the hinge line of the body flap as expected. The very slight divergence of the skin-friction lines at the symmetry line results there in a somewhat smaller reduction of T_{ra}, Fig. 6.25. On the flap the temperature is about 1,000 K higher in both cases. The expected decrease of T_{ra} on the flap in downstream direction is indicated, however, with the given data we cannot verify the $x^{-0.05}$ behavior which we expect for turbulent flow.

Non-convex effects show up other than anticipated. On the flap, the temperature is hardly affected at all. On the lower side of the vehicle ahead of the hinge line, the effect is rather strong with $\Delta T_{ra} \approx 100$–$150$ K, with only a weak influence on the separation behavior. Obviously the high surface temperature on the flap causes a stronger reduction of the effective emissivity on the lower side of the vehicle than vice versa. For details in this regard see [10]. Because the separation behavior is not much affected by the increase of the wall temperature in the onset flow region, the flap effectiveness is not reduced. However,

Table 6.11. Flight parameters of the numerical simulation of the flow past the X-38 configuration, [37].

Case	M_∞	H [km]	$Re_{L,\infty}$	L [m]	α [°]	η_{bf} [°]	$x/L\|_{trans}$	ε_0
2	15	54.1	$1.52{\cdot}10^6$	8.33	40.0	+20.0	fully turbulent	0.8
3	17.5	58.8	$1.02{\cdot}10^6$	8.33	40.0	+20.0	fully laminar/flap turbulent	0.8

the layout of the TPS on the lower side of the vehicle would need to take into account such a large ΔT_{ra}.

Figure 6.25 with the spanwise temperature distributions at position 1 in the onset flow regime, and at position 2 on the body flap (left side with constant emissivity, right side with non-convex effects) also shows another effect. At the side edge of the flap, visible also in Fig. 6.25, a strong temperature rise occurs in both cases (upper curves). This is due to the acceleration of the flow into the gap which leads to a thinning of the boundary layer. The corresponding weaker rise at position 1 (lower curves) is caused by the three-dimensionality of the onset flow.

Even if we have reservations regarding the performance of the basic k–ω model[27] and the mesh independence of the solution [12], the results show us what to expect from non-convex effects qualitatively and quantitatively. In any case they must be regarded, because thermal loads should be known as exact as possible for the TPS layout.[28]

Strong non-convex effects occur at the upper (leeward) side of the split body flap/elevon of the X-38, Sub-Section 3.3.5, i.e., the cavity region at the rear, Fig. 6.26. We discuss some results of an exploratory study [37, 38], keeping in mind the limitations due to turbulence modeling and grid sensitivity. Table 6.11 shows the flight conditions of the from [37] selected flight cases 2 and 3. The basic emissivity coefficient of the surface material was chosen to be $\varepsilon_0 = 0.8$, the effective surface emissivity coefficient ε_{eff} again was determined with the help of the GETHRA code. The computed surface-pressure distribution and the skin friction lines on the left part of the base area of the vehicle, on the left body flap, and in the cavity above the body flap are given in Fig. 6.27 for case 2. The skin friction topology in the cavity, although not well discernible, indicates the flow around the side edges of the flap and convergence to the attachment line present at the rear surface of the vehicle. The figure illustrates also well the hypersonic shadow effect at the base area of the flight vehicle with $p = p_w \approx 0.02$ to $0.3\,p_\infty$ at the middle axis of the area, and similarly at the blunt trailing edges of the winglets.

[27] The deflection angle of the body flap with $\eta_{bf} = +40°$ is very large, however the onset flow Mach number is with $M_{e,onset} \lessapprox 3.5$ small enough such that compressibility effects should not play a role.

[28] Note that at this unrealistically large deflection angle, the surface temperatures at the flap are at or beyond the limits of present-day materials, Fig. 6.25.

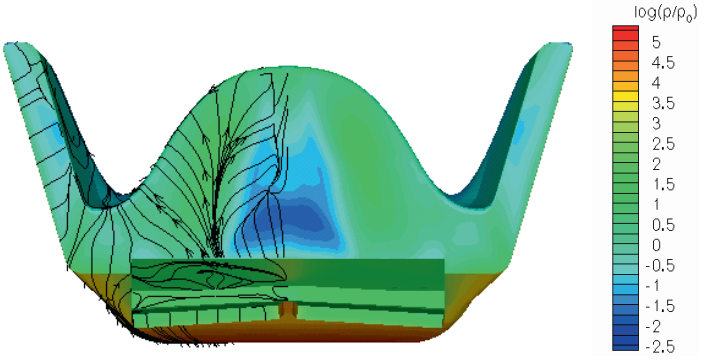

Fig. 6.27. Rear view of the X-38 with the surface-pressure distribution and skin-friction lines on the left part of the base area of the vehicle, on the body flap, and in the cavity above the split body flap/elevon, case 2, Table 6.11 [37]. Computation with ε_{eff}, $p_0 \equiv p_\infty$.

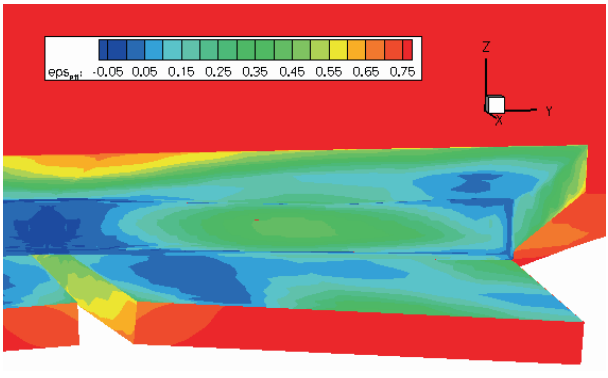

Fig. 6.28. Rear into the right-hand side part of the cavity of the X-38 with the distribution of the resulting effective surface emissivity ε_{eff}, case 2, Table 6.11 [37].

The resulting ε_{eff} distribution in the cavity is shown in Fig. 6.28. Note the low values along the cavity corners and especially in the vicinity of the middle gap, where even a small negative effective emissivity is indicated. At the middle of the forward wall of the cavity a region with larger ε_{eff} points to the possibility of a less impeded surface radiation.

However, looking at the ε_{eff} distribution one must remember that the actual radiation-adiabatic wall temperature distribution affects the effective emissivity [10]. This temperature distribution itself originates from the local boundary layer properties, which in turn are affected by the restricted radiation cooling. These non-linear couplings of several phenomena make a simple and comprehensive explanation of the result nearly impossible.

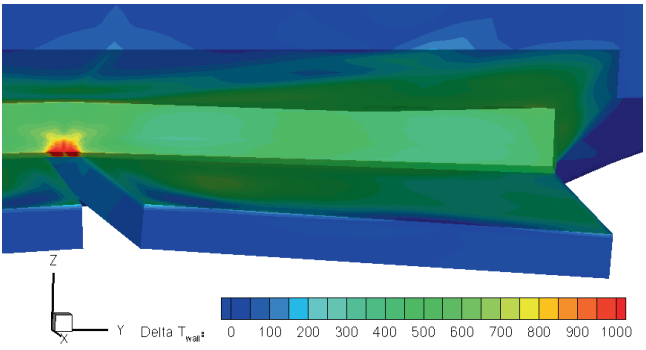

Fig. 6.29. Rear view into the cavity on the right-hand side of the X-38 with the distribution of the resulting ΔT_{wall} due to non-convex effects, case 2, Table 6.11 [37]. The reference temperature distribution is that found with $\varepsilon_0 = 0.8$.

Finally, in order to emphasize the effect, we show in Fig. 6.29 the resulting $\Delta T_{wall} = T_{wall,\varepsilon_{eff}} - T_{wall,\varepsilon_0}$ in the cavity. For the cavity forward wall, with exception of a small peak at the symmetry plane, an average jump in wall temperature of about 500 K results when we switch from $\varepsilon_0 = 0.8$ to ε_{eff}. Along the cavity ceiling the rise in temperature decreases from the forward outboard corners with $\Delta T_{wall} \approx 500$ K to values of about 100 K when approaching the rear end and the symmetry plane. The absolute values are $T_{wall,\varepsilon_{eff}} \approx 900$ K to 1,200 K.

The leeward side of the body flap shows some variations of ΔT_{wall} and a maximum temperature increase of about 500 K located at the inboard half of the surface. At the outboard half the average temperature rise is about 250 K. Along the body flap inboard side-edge, like at the blunt trailing edge, ΔT_{wall} is in the range of 100–250 K with the maximum values reached when approaching the body flap hinge line. The largest ΔT_{wall} appears in a small portion of the cavity front wall just in front of the gap between the two split body flaps. In this place it reaches up to 1,000 K. This peak seems to be due to the particular surface and grid characteristics used for the computations.

In [37], an attempt was made to simulate the influence of transverse heat transfer from the windward to the leeward sides of the split flaps for case 3 in Table 6.11. The windward side temperature, ranging from $T_{wall} \approx 1,600$ K to 1,950 K, was simply imposed on the leeside surface of the flap. This resulted in a partly large increase of the surface temperature at the cavity ceiling with a number of severe hot-spot locations, reaching almost the radiation-adiabatic temperature at the forward stagnation point of the vehicle, Fig. 6.30.

So far we have considered either fully laminar or fully turbulent flow past control surfaces. If laminar–turbulent transition occurs in the interaction domain around the hinge line, the situation will become complicated. The experimental or theoretical/numerical prediction of the location and the extent of the transition region in attached viscous flow is still unreliable and inaccu-

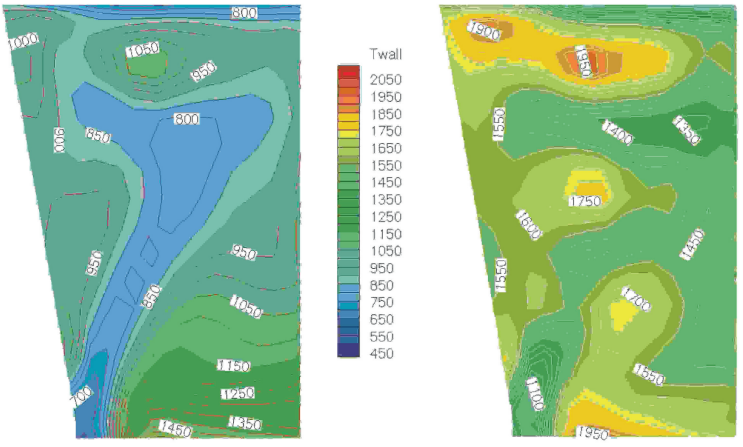

Fig. 6.30. Transverse heat transfer: distribution of the radiation-adiabatic wall temperature $T_{wall} \equiv T_{ra}$ at the ceiling of the cavity above the left body flap, case 3, Table 6.11 [37]. Left part of the figure: reference computation with ε_{eff}, right part: computation with ε_{eff} and temperature of the windward side of the body flap imposed on the lee side. View of the ceiling from below, the right-hand side edges of the figures corresponds to the flaps trailing edges, the lower edges to the (middle) gap sides.

rate [10]. This holds in particular when transition occurs in a flow domain with strong interaction and flow separation phenomena.

Transition in the interaction domain will affect especially the behavior of the thermal state of the ramp surface as well as the wall shear stress. If, for instance, separation occurs around the hinge line, case c), Fig. 6.9, transition may occur already in the free shear layer upstream or close to the reattachment point A.[29] This was observed in the Space Shuttle Orbiter where the flow past the deflected body flap became transitional, at very large Mach numbers, long before transition occurred on the vehicle's windward side [23]. In such cases the heat transfer may become even larger than for fully turbulent flow [29]. Responsible for this is probably a thinning of the reattached boundary layer, also Görtler phenomena most likely play a role.

The occurrence of Görtler vortices [8, 39, 40] mentioned on page 295 is a particular problem. These vortices are due to a centrifugal instability [10]. They can appear in concave flow situations like at a flat-plate/ramp (compression corner) configuration in laminar flow, transitional and even turbulent flow; for the latter, see [3]. In hypersonic flow, they can lead to the phenomenon of striation heating, i.e., transversal heat-flux variations. Results of a parametric study in [29] point to a bounding of these variations by the local turbulent heating level, if the flow would be turbulent. They decay to zero, when fully turbulent flow is attained over the entire ramp surface.

[29] This is a phenomenon similar to bubble transition downstream of the suction peak of an airfoil.

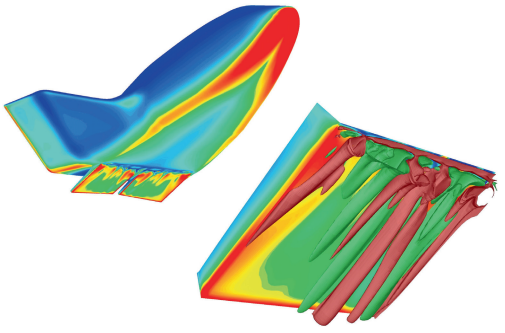

Fig. 6.31. Numerical simulation of striation heating on the split body flap, $\eta_{bf} = 20°$, of the X-38 (left part), and visualization (with exaggeration of the thickness of the flow features) of the streamwise Görtler vortices on the left flap (right part) [42].

We close this part by showing the result of a numerical study, [41, 38] of the flow past the split body flap/elevon, $\eta_{bf} = 20°$ of the X-38 with Görtler vortices, Fig. 6.31 [42]. It was possible to simulate the striation heating due to these vortices in laminar as well as transitional flow by employing in the flap region strongly refined computational grids in the spanwise direction.

In the left part of Fig. 6.31, striation heating on the flap surfaces, generated by the geometrically triggered vortices is shown for a case with otherwise fully laminar flow. In the right part, surface contours of the streamwise perturbation velocity in the flow past the left flap are shown, with exaggerated features for a better view, which are the indicator of the presence of vortex-like disturbances. Note in the left part of the figure the large heat flux in the nose region as well as along the left and the right primary attachment lines, which is due to the thinning of the boundary layer, attributable to the flow divergence occurring there [10].

The discussions in this part have shown that an asymptotic thermal state of the surface can be expected on a flap with optimal onset flow geometry, as long as the flow is two-dimensional, or at most only weakly three-dimensional. Unfortunately the basis of well suited experimental data is small and partly restricted to the immediate vicinity of the strong interaction domain around the hinge line.

The potentially important influence of non-convex effects of surface radiation cooling on the thermal state of the surface has been demonstrated with computational data, especially for the complex cavity above the split body flap of the X-38.

In general it must be noted that turbulent and more so transitional flow states make the numerical, but to a large degree also the experimental, simulation of control-surface flow problematic. Hence thermal loads cannot yet be predicted with the desired reliability and accuracy.

6.3.4 Behavior of the Wall-Shear Stress

The wall-shear stress exerted by the flow past the aerodynamic control surface is of large importance, if the flap material, and its coating, respectively, is thermally highly stressed. The coating of, for instance a body flap, has anti-oxidation, low catalycity, and high thermal emissivity properties, which must not be degraded by erosion processes due to the skin-friction.

If separation happens around the hinge line of the control surface, case c), Fig. 6.9, the wall-shear stress certainly is small in that region. However, downstream of the reattachment point A it will initially be large. The asymptotic behavior, found with the reference-temperature approximation, then is $\tau_w \sim x^{-n}$, Sub-Section 10.4.3. We note in addition, that the wall-shear stress depends on the wall temperature, via the reference temperature, with $\tau_w \sim (T^*/T_e)^m$, where $m = n(1+\omega)-1$, which is always smaller one. Increasing T_w and hence T^* reduces τ_w. The effect is much stronger for turbulent flow, the exponent being there $m = -0.67$, than for laminar flow with $m = -0.175$, ω in both cases being 0.65, Section 10.2. Experimental and numerical data regarding the asymptotic behavior are available for the domain just downstream of the hinge line, respectively the reattachment point, but we do not pursue this topic further.

6.4 Hinge-Line Gap Flow Issues

Between the vehicle structure and the movable flap is a gap of a certain width, Fig. 6.1. Its role is to insure the movability of the flap. Flow through the hinge-line gap, called bleed-flow in the similar inlet ramp flow problem, Section 4.5.5, is of interest for several reasons: a) it can degrade flap effectiveness because it takes flow momentum away, b) it can improve flap effectiveness, if it removes low momentum boundary layer flow, and thus reduces separation around the hinge line, c) it is the source of large thermal loads on the structure surrounding the gap, because surface radiation cooling is not possible there.

Point b) is discussed in [23] as a possible means *to destroy separation and increase flap effectiveness.*[30] This may make necessary a hinge gap width larger than needed for flap movability. Then also inviscid flow may enter the gap, and the thermal loads problem is enhanced. The reason is, that this flow, other than the boundary layer flow, carries the original total enthalpy. Only the surface-near part of the boundary layer flow has lost total enthalpy due to surface radiation cooling.

A closer look at the problem shows that, if this is possible at all due to the overall layout of the flight vehicle, one should bleed away low-momentum boundary layer flow material already ahead of the hinge gap, rather than

[30] The reader is asked to recall the discussion of Fig. 6.10 on page 302 regarding the effect of separation.

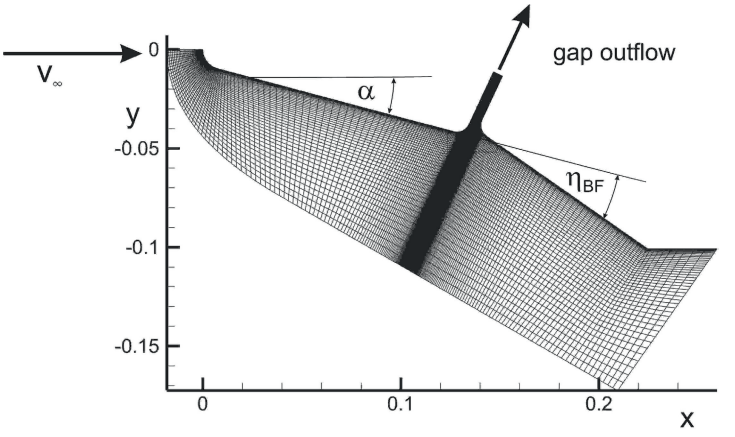

Fig. 6.32. Geometry and computational grid of the generic flap model [44], $\alpha = 15°$, $\eta_{bf} = +20°$, gap width 5 mm. The axis dimensions are given in meters.

Table 6.12. Flow conditions of the tests with the generic flap model in the plasma tunnel L3K of DLR [44]. Test gas is air.

M_∞	p_t [kPa]	T_t [K]	h_t [MJ/kg]	p_∞ [Pa]	ρ_∞ [kg/m^3]	T_∞ [K]	α [°]	η_{bf} [°]	ε_0
7.27	570.0	6,255.0	5.44	86	0.000387	620.0	15.0	+ 20.0	0.85

through it, Section 4.5.5. This would improve the momentum flux of the onset flow boundary layer. Tripping of the boundary layer is effective only at low boundary layer edge Mach numbers ($M_{e,onset} \lessapprox 5$). Therefore, it could be a remedy for flap separation when employed for re-entry vehicles, but not for CAV's or ARV's with large onset flow Mach numbers.

In the following, we discuss modeling issues of gap flow heating. The flow past the reference configuration 'X-38 body flap with hinge-line gap' was studied experimentally and numerically in the German TETRA Programme, Sub-Section 8.4.3. Geometry and arrangement of the partially cooled generic flap model [43], are shown in Fig. 8.19, the dimensions of the model and the (final) computational grid in Fig. 6.32 [44]. The width of the model was $w_{flap} = 0.144$ m.

The blunt nosed, flat plate part of the configuration was oriented at angle of attack $\alpha = 15°$ with the flap deflected with $\eta_{bf} = +20°$. The flow parameters are given in Table 6.12. The selected computation results discussed in the following were obtained assuming two-dimensional laminar flow, no-slip boundary conditions, and a non-equilibrium real-gas model with non-catalytic wall. The radiation-adiabatic surface boundary condition was employed, and non-convex effects were taken into account.

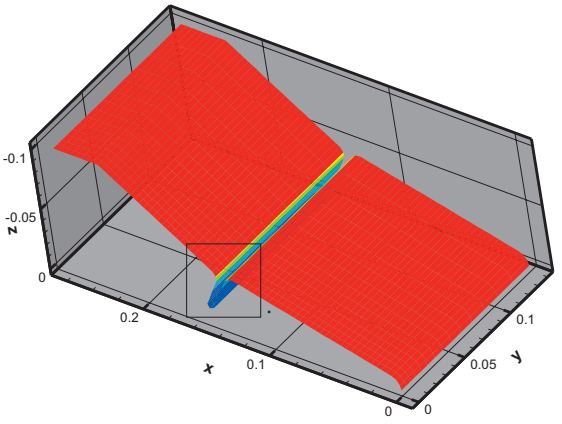

Fig. 6.33. Distribution of the initial effective emissivity coefficient ε_{eff} on the whole surface of the model, [38, 44]. The flow is coming from the right-hand side.

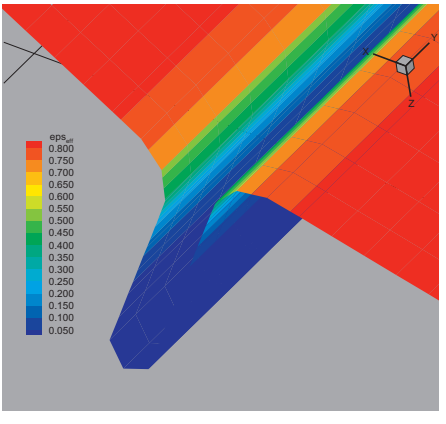

Fig. 6.34. Detail from Fig. 6.33: distribution of the initial effective emissivity coefficient ε_{eff} in the gap region, [38, 44].

The distribution of the effective emissivity coefficient ε_{eff} on the whole surface of the model is shown in Fig. 6.33. This is the initial ε_{eff} distribution, which was found assuming $T_w = 1,000$ K. It was updated during the computation with the actual computed radiation-adiabatic temperature distribution. The original material emissivity of the surface is $\varepsilon_0 = 0.85$. Radiation from the gap bottom was suppressed. Strong non-convex effects are observed only in the gap region, Fig. 6.34. The effective emissivity coefficient is seen to drop fast to almost zero deep in the gap, as is to be expected.

The open gap computations were made with an outlet pressure of 100 Pa. A change to 500 Pa had no noteworthy influence on the solution. We see in Fig. 6.35 at the left the high pressure at the blunt nose of the configuration. The

small kink at $x \approx 0.025$ m indicates the recompression shock due to the jump of the curvature at the blunt-nose/flat-plate junction. The pressure decreases slightly in downstream direction, pointing to possible hypersonic viscous interaction and blunt-nose effects. With closed gap the wall pressure departs at $x \approx 0.075$m where upstream separation occurs, Fig. 6.9c). The separation forms a pressure plateau ahead of the hinge line. Downstream of the hinge line, the pressure rises monotonically without reaching a ramp pressure plateau.

With an open gap the picture changes completely. Separation does not occur upstream of the hinge line, the wall pressure rises only weakly just ahead of the gap. In the gap a small separation bubble forms, see Fig. 8.20, Sub-Section 8.4.3. On the ramp then we have the pressure rise on a higher level than before. In general we find the situation mentioned on page 324 as point b), discussed in [23]: a wide enough gap around the hinge line takes away the upstream separation and, in addition, rises the flap pressure, thus increasing the flap effectiveness. A question not answered is, however, the asymptotic behavior, i.e., whether on a flap long enough with gap, the same pressure plateau is reached as without gap.

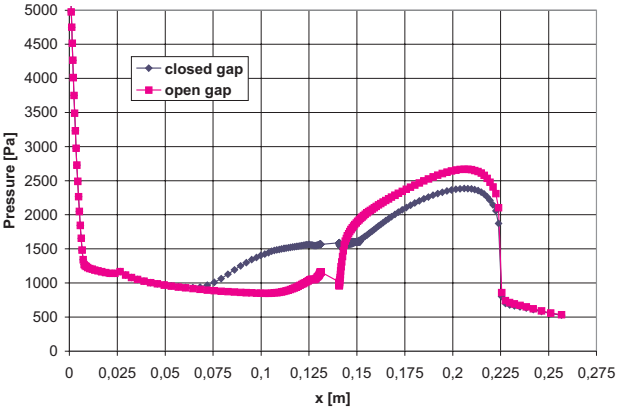

Fig. 6.35. Computed surface pressure distribution with closed and with open gap, gap region omitted [44].

This effect, however, is bought with the above mentioned increase of the thermal loads in the gap, point c), page 324. With closed gap, Fig. 6.36, we find the drop of the radiation-adiabatic wall temperature beginning at the location of separation, $x \approx 0.075$ m—compare with Fig. 6.12—which rises downstream of $x \approx 0.1$ m again to $T_{ra} \approx 1,000$ K just ahead of the gap. Downstream of the gap it rises to a peak at the end of the ramp part at $x = 0.225$ m of the configuration, without attaining on the ramp the asymptotic decrease as seen for instance in Figs. 6.20 and 6.21. At the right-hand side of the gap a small temperature peak, just below 1,200 K, is indicated.

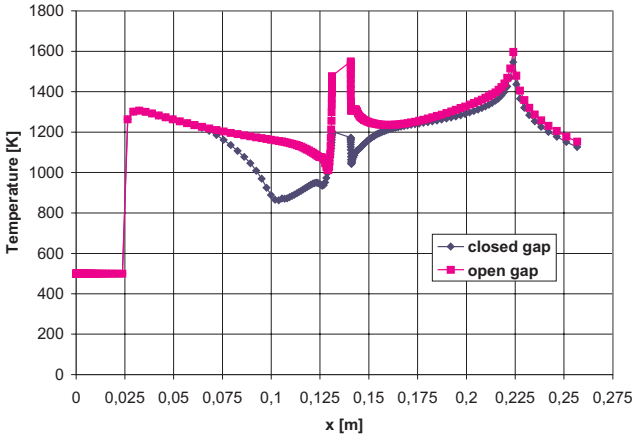

Fig. 6.36. Computed radiation-adiabatic surface temperature distribution with closed and with open gap, gap region omitted [44].

With an open gap the radiation-adiabatic temperature ahead of the hinge line follows longer than in the case without gap the $x^{-0.125}$ proportionality of laminar flow, Sub-Section 10.4.3, and then drops towards the small separation bubble at the forward wall of the gap, Fig. 8.20. Along the gap walls it reaches, as far it can be represented in Fig. 8.20, the expected high values, here 1,500–1,600 K. Downstream of the gap the temperature first drops and then rises similar as in the closed gap case, but with slightly larger values, towards the peak.

The experiment with the partially cooled ramp configuration was performed in the plasma tunnel L3K of DLR [43]. The steady state temperature distribution, reached after about 325 s, of course is different to that discussed above. To take the whole experimental situation into account, the multidisciplinary simulation sketched in Sub-Section 8.3.3 becomes necessary. It is shown there, see also, e.g., [45], that a three-dimensional flow-structure coupled simulation is necessary to capture the model-in-tunnel situation. Although the obtained accuracy was not yet satisfactory, see also Sub-Section 6.7.2, the modelling of the influence of heat conduction into the wind-tunnel model and a full description of flow three-dimensionality was deemed to be necessary. In a gap and its immediate vicinity, the radiation-adiabatic temperature, even with non-convex effects taken into account, is no more a sufficient and reliable approximation as it is in general for the thermal state of the wall of external radiation cooled vehicle surfaces [10]. This holds also for gaps of a TPS.

6.5 Aerothermodynamic Issues of Reaction Control Systems

Reaction control systems (RCS) of RV-W's and RV-NW's have two purposes:

- maneuvering of the vehicle in orbit, including the de-orbiting maneuver, where control forces cannot be generated aerodynamically,
- control of the vehicle during re-entry, Section 2.1, on at least a part of the trajectory (RV-W's), or on the whole trajectory (RV-NW's).

A RCS thruster produces either a force or a force and a moment on the vehicle. Side effects in orbital flight are, for instance:

- stray forces because of interaction with vehicle surfaces (jet impingement), Fig. 6.37 right,
- contamination of vehicle surfaces with plume constituents.

During re-entry flight these side effects can occur but other, more important effects are:

- amplification or even reduction of the thruster force by interaction with the flow field past the flight vehicle, Fig. 6.37 left,
- amplification of thermal loads on the vehicle structure, especially the creation of hot-spot situations by the said interaction.

RCS performance was shown for the Space Shuttle Orbiter in general to be predictable with the help of ground facility simulation [48]. Many studies of the jet/surface flow field interaction shown in Fig. 6.37 left, can be found in the literature [47]. Much data are available for both laminar and turbulent surface flow fields.

The first Orbiter flight however has revealed a particular problem related to the flow situation sketched in Fig. 6.37 right. It arose during the initial bank

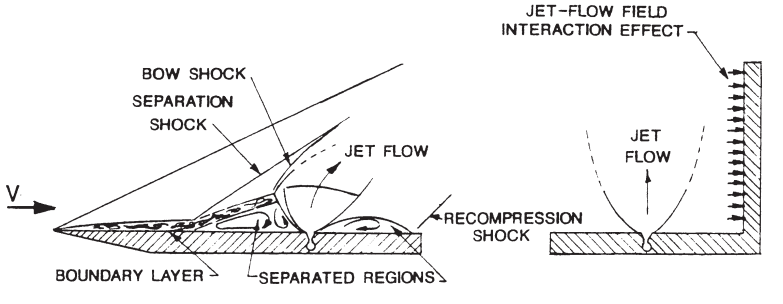

Fig. 6.37. Schematics of interactions of a RCS jet embedded in a supersonic flow field [46]. Left: interaction of the jet with the surface flow field [47], right: interaction of the jet with an adjacent surface.

maneuver with the side-firing RCS thruster housed in the Orbital Manoeuvering System (OMS) pod. The produced rolling moment was smaller than predicted. The sketch in Fig. 6.37 right, is in so far misleading, as in this case at large flight Mach number and $\alpha \approx 40°$, the surface in question was the upper side of the wing. The flow above and behind the wing at this flight attitude is massively separated, Fig. 6.38, the Reynolds number is very small [46].

RCS performance for yaw and roll control of the Space Shuttle Orbiter, as we have noted in Chapter 2, is needed due to its central vertical stabilizer (and rudder) down to flight Mach numbers $M_\infty \approx 1$. Ground simulation of RCS for yaw and roll control is complicated by the large Mach/Reynolds number span present together with changing free-stream dynamic pressure and large angles of attack.

We do not attempt to discuss here the flow phenomena and simulation issues of this particular problem. We restrict ourselves in the following to the discussion and illustration of the basic interaction phenomena, Fig. 6.37 left, of reaction control systems during re-entry flight of the vehicle. We do this in view of thruster force amplification/reduction and thermal loads amplification at two different locations of the X-38 configuration. The material and the data stem from computational studies performed in the frame of the German national technology programme ASTRA [49]–[51].

The flight parameters are given in Table 6.13. The combinations of angle of attack, thruster and thruster locations, Tables 6.15 and 6.14, do not reflect flight situations. They were chosen, in view of the influence of the onset flow, such that different jet/flow field interactions occur, the strongest in case 1, the weakest in case 3.

Two thrusters at different locations at the front part of the vehicle were considered, Fig. 6.39. Thruster 1 has a nominal design thrust of 110 N, and thruster 2 of 400 N, Table 6.15. The location of thruster 1 is the original one. The location of thruster 2, of course is an unlikely one, but it was chosen in comparison to that of thruster 1 such that:

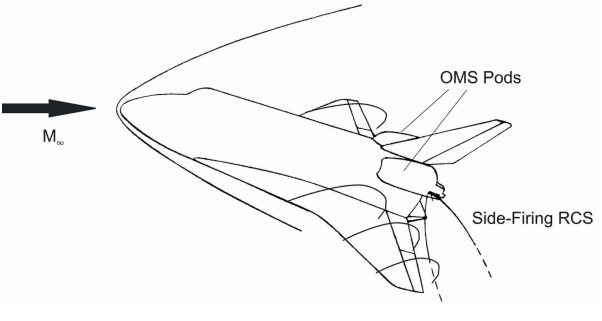

Fig. 6.38. Sketch of the side-firing jet situation at the Space Shuttle Orbiter at $\alpha \approx 40°$ [46].

Table 6.13. Flight parameters of the computational study of jet/flow field interaction at the X-38 configuration, [49]. The flow is assumed to be laminar and in thermo-chemical equilibrium. No-slip and radiation-adiabatic boundary conditions are applied at the vehicle's surface.

Case	M_∞	H [km]	p_∞ [Pa]	T_∞ [K]	ρ_∞ [kg/m^3]	L [m]	ε	Thruster	α [°]
1	17.5	58.8	26.19	258.08	$3.546{\cdot}10^{-4}$	8.33	0.8	1	0.0
2	17.5	58.8	26.19	258.08	$3.546{\cdot}10^{-4}$	8.33	0.8	2	0.0
3	17.5	58.8	26.19	258.08	$3.546{\cdot}10^{-4}$	8.33	0.8	2	40.0

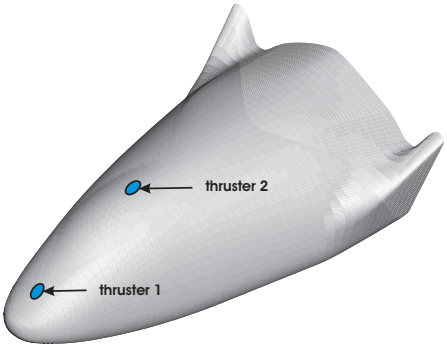

Fig. 6.39. Locations of the thrusters for the X-38 [49].

Table 6.14. The geometrical data of the thrusters of the computational study of jet/flow field interaction at the X-38 configuration [49]. The distance to the reference point is denoted with Δx.

Thruster	Exit diameter	Exit area A_{exit}	x-position	Δx
1	17.13 mm	$2.30{\cdot}10^{-4}$ m^2	0.6351 m	4.16 m
2	244.0 mm	$4.68{\cdot}10^{-2}$ m^2	2.5237 m	2.2714 m

– the vehicle surface at that position is less curved longitudinally,
– a different jet/flow field interaction occurs,
– the vehicle reaction moments are similar.

The geometrical data of the thrusters are shown in Table 6.14. The coordinates of the reference point, the center-of-gravity of the flight vehicle, are: $x_{ref} = 4.7951$ m, $y_{ref} = 0$ m, $z_{ref} = 0.8042$ m, with the origin of the coordinate system lying 15.24 cm ahead of the nose point in the lower-side plane of the vehicle. The exit planes of the thrusters are flush with the vehicle surface, the nozzle axes are oriented parallel to the z-axis of the vehicle. The thruster jets are assumed to leave their nozzles without profile and boundary layer. The

thruster flow parameters are given in Table 6.15. The thrust $F_{z,jet} = |\underline{F}_{z,jet}|$ was computed with

$$F_{z,jet} = \dot{m}\, u_{exit} + (p_{exit} - p_{env})\, A_{exit}, \tag{6.11}$$

where the environment (ambient) pressure was chosen to be $p_{env} = 0$ Pa.

In the following we discuss selected results from [49, 50]. We have first a look at results from a test case presented in [50]. It was computed with the parameters from case 2, Table 6.13, with the thruster located on a flat surface. The jet's exit pressure was ten times enlarged in order to enhance its influence on the surface flow field.

In Fig. 6.40, the surface pressure, skin-friction lines and, in the symmetry plane, the jet and streamlines are shown. The strong jet leaves the surface perpendicular, the surface flow comes from the lower right side. We see the primary separation line ahead of the jet, the separation shock, the (primary) flat horseshoe vortex, the primary attachment line, and then, directly ahead of the jet, a secondary, small horseshoe vortex. Compare this to the cross-section view in Fig. 6.37 left. This secondary, small horseshoe vortex is directly driven by the jet. The skin-friction lines go around the jet, and finally a separation line indicates the separation region behind the jet. Well discernible is the pressure minimum induced by the primary horse-shoe vortex, as well as the relative pressure maximum along and around the attachment line, which is typical for any attachment line.

The flow situation of the test case is found approximately also in case 1 of Table 6.13, Fig. 6.41. Here we look from above on the surface. On the right-hand side the skin-friction lines and the radiation-adiabatic temperature without thruster are shown. At $\alpha = 0°$, the position of thruster 1, Fig. 6.39, is directly impacted by the flow and hence the surface temperatures are around 1,600 K.

The left-hand side of the figure now shows a remarkable amplification and variation of the surface temperature due to the jet/flow field interaction. The divergent flow at the (primary) attachment line causes a strong thinning of the viscous flow, which leads to a local hot-spot situation with radiation-adiabatic temperatures around 2,500 K, whereas on a large surface portion downstream of it temperatures around 2,000 K are found. At the primary separation line ahead of the jet, below the primary horseshoe vortex, and also directly behind the jet, cold-spot situations with temperatures around 1,300 K are indicated.

Table 6.15. Thruster flow parameters (operational environment) of the computational study of jet/flow field interaction at the X-38 configuration [49].

Thruster	p_{exit} [Pa]	T_{exit} [K]	u_{exit} [m/s]	M_{exit} [−]	$\dot{m}$ [kg/s]	$F_{z,jet}$ [N]
1	16,210.0	56.5	640.5	4.25	0.148	98.5
2	192.1	728.5	3,243.4	5.99	0.139	459.8

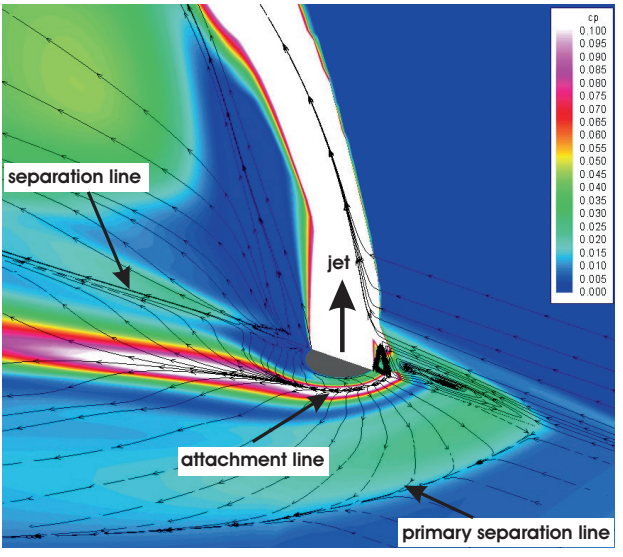

Fig. 6.40. Case 2: thruster 2 with $p_{exit} = 1,921$ Pa, perfect gas assumption and flat surface (test case): pressure iso-surfaces, streamlines and skin-friction lines [49, 50]. The main flow direction is from the lower right to the upper left side.

For case 2 of Table 6.13, Fig. 6.42, we observe a pattern different to that of case 1, Fig. 6.41. The temperature field on the right-hand side indicates that thruster 2, with a jet stronger than that of case 1, Table 6.15, lies already somewhat in the hypersonic shadow of the fuselage. Consequently no upstream jet/flow field interaction occurs (left side of Fig. 6.42). The streamlines directly ahead of the jet are straight. This points to a low-momentum onset flow and an ejector-like effect of the jet. Of particular interest are here the hot-spot situations. We find such a situation directly at the jet, and then behind the jet along part of the symmetry line, where the attachment line shows a strong divergence of the skin-friction lines. The ensuing temperatures are about 500 K larger than without jet.

We observe low-momentum onset flow and an ejector-like effect of the jet also for case 3 of Table 6.13 in Fig. 6.43. The onset flow of the jet is even less affected by the jet. The reason is, that now, at $\alpha = 40°$, the thruster location is fully in the hypersonic shadow of the fuselage, and, as indicated at the right-hand side of the figure, at the beginning of a lee-side separation domain.

The global separation line, being the primary separation line at the upper part of the fuselage, Fig. 6.43, right side, leads to a well pronounced cold-spot situation. This is asymmetric, because of the different properties of the two boundary layers involved in this primary separation, which is of "open separation" type [52]; see also the discussion of the Blunt Delta Wing (BDW) exam-

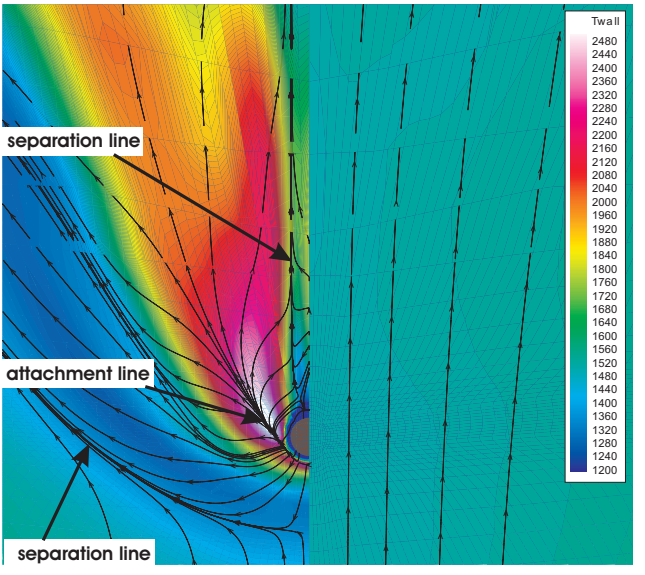

Fig. 6.41. Case 1: X-38 surface with temperature iso-surfaces and skin-friction lines, $\alpha = 0°$. Left side: flow field with thruster 1, right side: flow field without thruster [49]–[51].

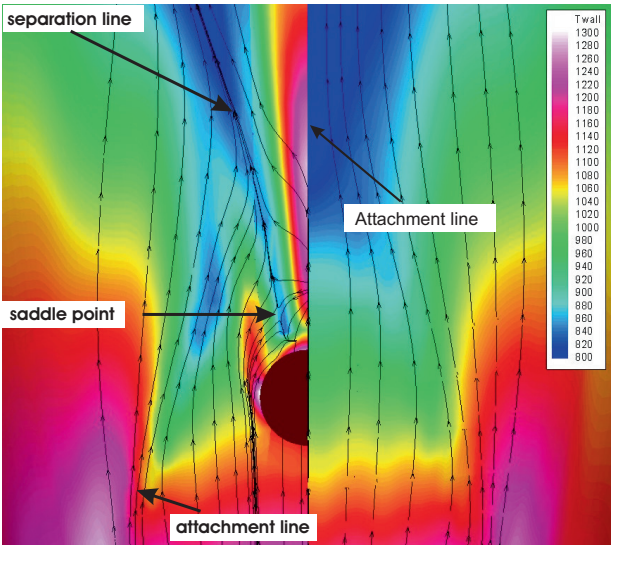

Fig. 6.42. Case 2: X-38 surface with temperature iso-surfaces and skin-friction lines, $\alpha = 0°$. Left side: flow field with thruster 2, right side: flow field without thruster [49, 50]. The color code of the surface temperature is different from that in the other figures.

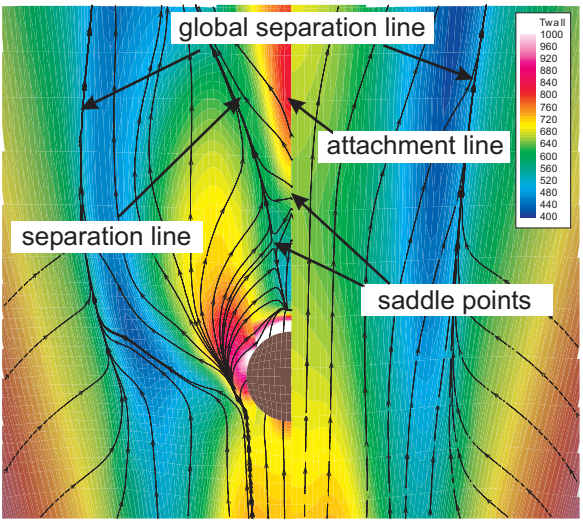

Fig. 6.43. Case 3: X-38 surface with temperature iso-surfaces and skin-friction lines, $\alpha = 40°$. Left side: flow field with thruster 2, right side: flow field without thruster [49, 50]. The color code of the surface temperature is different from that in the other figures.

Table 6.16. Normal forces F_z ($\equiv N$) and pitching moment coefficients C_m of the X-38 configuration with and without thruster jet [49].

Case	α [°]	Thruster	$F_{z,jet}$ [N]	F_z [N]	C_m [–]
–	0.0	no	0.0	−3, 920.88	0.00213
1	0.0	1	−98.5	−4, 155.80	0.00196
2	0.0	2	−459.8	−4, 312.10	0.00129
–	40.0	no	0.0	65,955,20	0.0653
3	40.0	2	−459.8	65,475.62	0.0643

ple in [10]. The left-hand side of Fig. 6.43 still shows the open-separation type, although distorted by the jet action.

At the side of the jet we see an attachment line like pattern of the skin-friction lines, accompanied by a hot-spot situation, which increases towards the rear part of the jet. Due to the particular skin-friction line topology, with an attachment point approximately 1.5 jet diameters behind the jet, an attachment line ensues along the symmetry line downstream of this point. It leads also to a hot-spot situation. This is remarkable in so far, as it lies at a rather large distance from the jet.

We come now to the topic of amplification of the jet performance. Integration of the surface pressure of the configuration yields the force F_z ($\equiv N$) in

z-direction (body-fixed coordinate system) and the pitching moment M. In Table 6.16 we give the resulting forces F_z with and without the thruster jet forces $F_{z,jet} = -F_{thruster\,jet}$, Table 6.15, and the pitching moment coefficient C_m. As was mentioned above, the interaction of the jet with the flow field can amplify or reduce the thruster force. The thrust amplification factor A_{F_z} is defined as

$$A_{F_z} = \frac{F_{z,config,with\,jet} - F_{z,config,without\,jet}}{F_{z,jet}}, \tag{6.12}$$

where $F_{z,config,with\,jet}$ denotes the aerodynamic force with working thruster and $F_{z,config,without\,jet}$ that without working thruster.

With the forces from Table 6.16, we find the amplification factors in Table 6.17. In case 1, with strong jet/flow field interaction, we find an amplification larger than two. The smaller interaction in case 2, where the jet is deflected such that it impinges on the surface [49], leads to an attenuation. In case 3, where the jet is fully in the hypersonic shadow, the interaction is weaker, but the jet is not deflected down to the surface. Here we get a small amplification. The pitching moment coefficient C_m is reduced accordingly with approximately seven per cent in case 1, forty per cent in case 2, and two per cent in case 3.

Table 6.17. Thruster amplification factors A_{F_z} from the computational study of jet/flow field interaction at the X-38 configuration, [49].

Case	α [°]	Thruster	A_{F_z} [−]
1	0.0	1	2.38
2	0.0	2	0.85
3	40.0	2	1.04

6.6 Configurational Considerations

Hypersonic vehicles of either type basically have the same stabilization, trim, and control surfaces which ordinary aircraft have. Elevators, ailerons, and rudders are control surfaces for pitch, roll, and yaw motion, respectively. Functions may be combined in multi-functional control surfaces, while in special arrangements control surfaces may serve as airbrakes for energy modulation, too. Longitudinal trim can be achieved with elevators and ailerons together. For RV-W-type vehicles, however, the Space Shuttle Orbiter did set a precedent by using the body flap as primary longitudinal trim device. Originally it was to act as a heat shield for the main engines nozzles only.

Both the blunt RV-W and the slender CAV usually have delta or double-delta shaped wings[31] which are fully blended with the fuselage at least on the lower (windward) side. The limiting case of RV-W's is the lifting body, such as the X-38, with restricted cross-range capabilities, Section 2.1 because of a small lift-to-drag ratio, and limited low-speed properties. In neither flight vehicle class is a horizontal tail unit found as for subsonic and transonic aircraft. The reasons are the large thermal loads, structural weight considerations and, with CAV's, propulsion integration issues; last, but not least the low and critical stability contributions of tail units in combination with low aspect-ratio wings.

6.6.1 Examples of Stabilization, Trim and Control Devices

Aerodynamic pitch trim of RV-W's usually is made with the body flap, Fig. 6.44a) and b). Longitudinal control is achieved by means of so-called elevons. These are multi-functional devices which act as elevators (symmetric deflection for pitch control) or ailerons (asymmetric deflection for roll control). On the Orbiter and the HOPPER configuration, they are located at the wing's trailing edges and split into outboard and inboard surfaces, Fig. 6.44a) and b). A special case is the X-38, Fig. 6.44c). Here, two surfaces at the lower end of the vehicle act as split body flap and elevons.

Aerodynamic yaw (directional) stability and control of RV-W's is achieved with the help of single or dual vertical stabilizer surfaces and rudders, located at the back of the upper side of the vehicle, Fig. 6.44. The Orbiter and the HOPPER configuration have a single vertical stabilizer, the X-38 has a dual vertical stabilizer in the form of wing-tip surfaces. Such wing-tip solutions are also found on a number of older vehicle projects [23], and also on the European HERMES vehicle.

Roll control is made, with the elevons in aileron function, in addition with the rudder(s) at high angles of attack (avoidance of adverse yaw-roll coupling), roll damping is mainly achieved with the wing. The rudder of the Orbiter is a split control surface. Both panels deflected together in the same direction act as rudder for yaw control, and deflected symmetrically to the left and the right as speed brake (air brake) for drag modulation. The HOPPER configuration has speed brakes at the sides of the aft fuselage.

As was noted and discussed in Sub-Section 2.1.2 and in Section 6.5, RV-W's need a reaction control system for different stabilization and control objectives on parts of the re-entry trajectory. We show as example in Fig. 6.45 the configuration of the Space Shuttle Orbiter's RCS for pitch, yaw, and roll control.

Aerodynamic trim, stabilization and control of CAV's and ARV's is made basically with the same surfaces as we have seen on RV-W's. However, the trim

[31] Such shapes provide large leading edge sweep for high speed (supersonic and hypersonic) flight and lead to the necessary low-speed properties of the low-aspect ratio wings. In the case of CAV's, these wing planforms permit also the control of the neutral-point shift with flight Mach number.

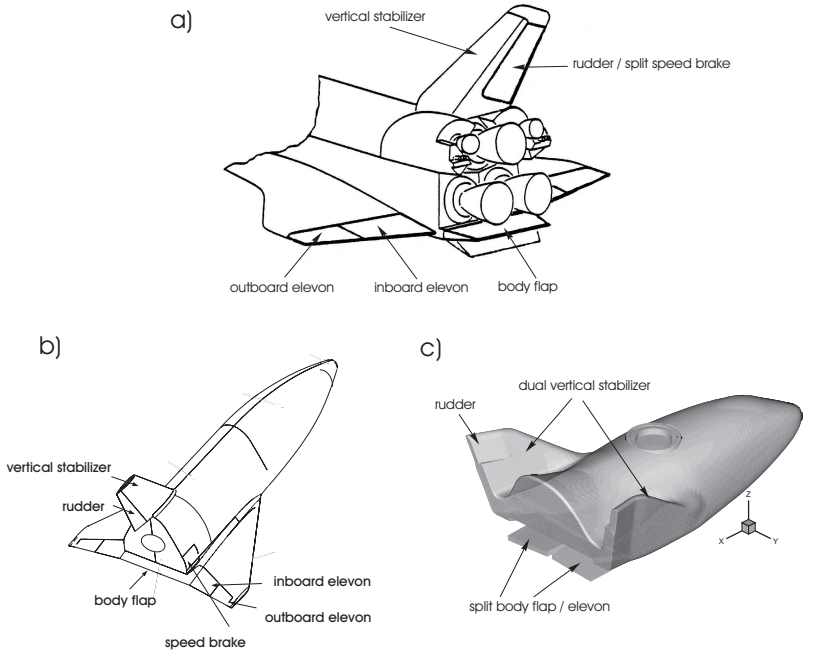

Fig. 6.44. Trim, stabilization, and control surfaces of a) the Space Shuttle Orbiter[53] (body flap shown in two positions), b) HOPPER, and c) X-38. Deflection and hinge moments characteristics of the Orbiter surfaces are given in Table 6.18.

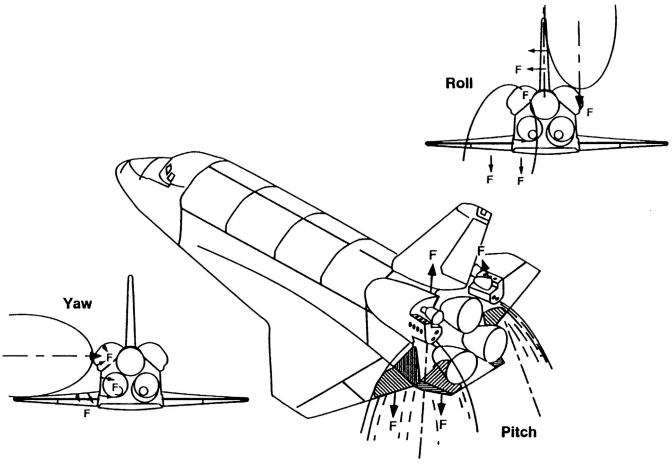

Fig. 6.45. The aft mounted reaction control system of the Space Shuttle Orbiter [54].

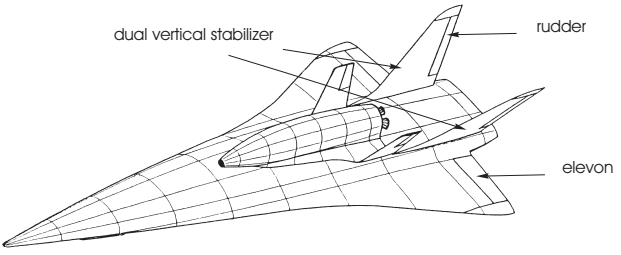

Fig. 6.46. Stabilization and trim/control surfaces of the lower stage of the TSTO system SÄNGER [55]. The upper side of the vehicle is shown with the upper stage HORUS.

surface (body flap) function usually is taken over by the elevon surfaces, with a strong coupling with the thrust vector, Sub-Section 2.2.3. A dual vertical stabilizer was foreseen, for instance, for the lower stage of SÄNGER, Fig. 6.46.

6.6.2 Geometrical Considerations

The overall geometrical peculiarities of hypersonic vehicles tell us, that the so called flap volume, the product of flap surface (plan area) times the distance (moment arm) from its center-of-pressure to the respective axis, which is oriented at the center-of-gravity of the flight vehicle, as a rule is rather small. This in general holds for all three axes and for stabilization surfaces, too. For either vehicle class the center-of-gravity is located rather far back. Characteristic numbers for RV-W's are 57 to 70 per cent aft position, Table 3.3. HORUS, the upper stage of the TSTO space transportation system SÄNGER, carries both hydrogen and oxygen for its ascent after separation from the lower airbreathing stage, and thus was projected to have a center-of-gravity location of approximately 54 per cent aft position at launch and approximately 60 per cent at re-entry [55].

The situation is different with airbreathing CAV's. Here the center-of-gravity position is more aft due to the location of the propulsion package. For the SÄNGER lower stage alone but with fuel, for instance, we find approximately 70 per cent, and for the whole TSTO-system at upper stage separation (nominal at $M_\infty = 6.7$) approximately 73–74 per cent [55]. Moreover, for faster hypersonic aircraft, this may change, Fig. 4.25, because the surface of the asymmetric external nozzle (single expansion ramp) of airbreathing CAV-type vehicles increases with increasing flight Mach number, [56]. Therefore with higher design flight Mach number the propulsion package, and hence the center-of-gravity will be located more forward.

The small moment arms, which we generally find on aerospace vehicles, compared to those of ordinary aircraft, demand stabilization or control surfaces which generate large forces. This can be achieved with a large size and/or,

Table 6.18. Deflection and hinge moments characteristics of the Space Shuttle Orbiter's aerodynamic trim and control surfaces, [57]. Upward moments like downward deflection angles are counted positive, see also Fig. 6.47.

Device	Deflection angle [°]	Deflection rate [°/s]	Hinge Moment [mN]
Body flap	+22.5 to −11.7	1 to 3	$> -158,172.0$
Inboard elevon as elevator	+20 to −35	20	$-103,150.7$ to $+89,932.1$
as aileron	+10 to −10	20	$-103,150.7$ to $+89,932.1$
Outboard elevon as elevator	+20 to −35	20	$-49,372.0$ to $+43,610.0$
as aileron	+10 to −10	20	$-49,372.0$ to $+43,610.0$
Rudder	+27.1 to −27.1	14	$< +90,384.0$
Speed brake	0 to +98.6	6 to 11	$> +282,450.0$

regarding only control and trim surfaces, with large deflection angles[32]. Concerning their size, stabilization and control surfaces must fit into the general layout of the flight vehicle. To get sufficient flap effectiveness at large deflection angles demands appropriate flap sizes and aspect ratios, too. Structural weight is another concern, and finally weight, volume, performance (hinge moments, flap deflection rates), and the energy demand of the actuators of the control surfaces require special attention.

As example for the demands on the actuators of a RV-W, deflection and hinge moment characteristics of the Space Shuttle Orbiter.[33] are given in Table 6.18. Deflection rates are generally small. In contrast to them, those of modern, unstable flying fighter aircraft are up to 80°/s.

6.6.3 Flap Width versus Flap Length

Regarding the geometry of an aerodynamic control surface, it is a question how to shape its planform best. In the following we study in particular the relation between its width and length (chord). A simple consideration reveals how moment arms, flap forces and moments are mutually connected. In Fig. 6.47 an idealized flight vehicle with a deflected control surface is shown. The latter has the length l_{flap} and the width (span) w_{flap}, the flap surface (plan area) is $l_{flap}\, w_{flap}$. The deflection angle is η.

[32] In general flap effectiveness encompasses the need for trim drag as small as possible in order not to compromise the effective lift-to-drag ratio of the flight vehicle, Chapter 2.

[33] Some of the characteristics, for instance the deflection angles, are cited somewhat differently in [53].

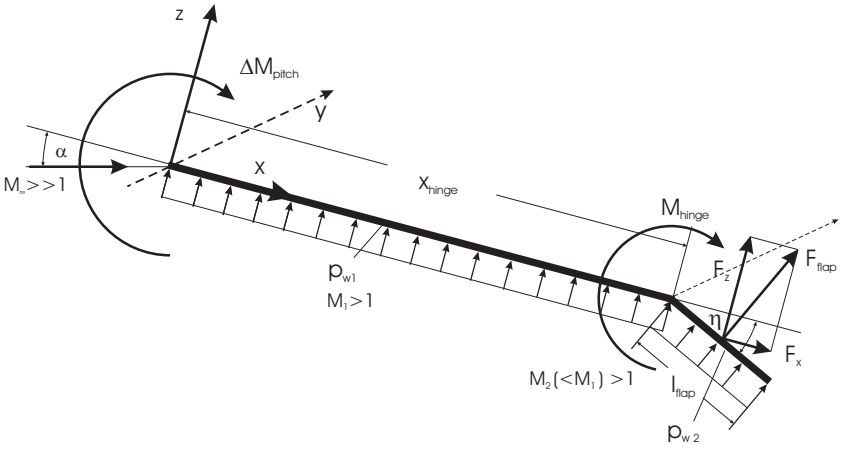

Fig. 6.47. Idealized hypersonic flight vehicle with deflected control surface, the generated flap force F_{flap}, the increment of the vehicle pitching moment ΔM_{pitch}, and the hinge moment M_{hinge}. It is assumed that a constant pressure p_{w_1} acts on the lower side of the flight vehicle, whereas a constant $p_{w_2} = p_{flap}$ acts on the lower side only of the deflected (η) control surface which has the dimensions length l_{flap} and width (span) w_{flap}. The lateral vehicle axis (y) is normal to the x–z plane.

We note that on a real vehicle x_{hinge} is the distance to the center-of-gravity, not to the vehicle nose, and that the center-of-pressure of the flap is not necessarily located at $0.5\, l_{flap}$.

We assume constant pressure p_{w_1} on the lower side of the flight vehicle. The pressure $p_{w_2} = p_{flap}$, acting only on the lower side of the flap, is also assumed to be constant.[34] The flap force F_{flap} is then

$$F_{flap} = l_{flap}\, w_{flap}\, p_{flap}. \tag{6.13}$$

It has the two components:

$$F_z = \cos\eta\, F_{flap},\ F_x = \sin\eta\, F_{flap}. \tag{6.14}$$

The flap force times its lever arm with respect to the vehicle's y-axis is balanced by the increment[35] of the vehicle moment ΔM_{pitch}:

[34] This is the ideal inviscid case. In reality the pressure on the flap will not be constant, and, if separation occurs around the hinge line, also the pressure on the lower side of the vehicle, just upstream of the hinge line, will not be constant, Sub-Section 6.3.2.

[35] It is customary to include, in the aerodynamic model of a flight vehicle, the increment due to a deflected flap in the overall moment around the respective axis. We deviate here from that custom in order to show more clearly the influence of the geometrical properties of a flap on the vehicle moment and the hinge moment.

$$\Delta M_{pitch} = -(x_{hinge} + \cos\eta \frac{l_{flap}}{2}) F_z - \sin\eta \frac{l_{flap}}{2} F_x. \tag{6.15}$$

If $l_{flap}/2 \ll x_{hinge}$ and for small to moderate deflection angles η, this reduces, with eq. (6.14) to

$$\Delta M_{pitch} = -x_{hinge}\, l_{flap}\, w_{flap}\, p_{flap}. \tag{6.16}$$

The flap force times its lever arm with respect to the flap axis now must be balanced by the hinge moment M_{hinge}

$$M_{hinge} = -\frac{l_{flap}}{2} F_{flap} = -\frac{l_{flap}^2}{2}\, w_{flap}\, p_{flap}. \tag{6.17}$$

We see from this simple consideration that $\Delta M_{pitch} \sim x_{hinge}\, l_{flap}\, w_{flap}$, whereas the hinge moment is $M_{hinge} \sim l_{flap}^2\, w_{flap}$. With regard to the demands on the actuator, this means that the flap length l_{flap}, because it appears quadratically, is more critical than the flap width w_{flap}. For the vehicle pitching moment the moment arm x_{hinge} is the governing length.

We conclude that a large x_{hinge} is beneficial for the vehicle pitching moment. Simultaneously, regarding the hinge moment, and hence the needed actuator performance, a large flap width w_{flap} is to be preferred rather than a large flap length l_{flap}. However, in any case a trade-off is necessary,[36] because with increasing flap length in general smaller deflection angles are needed (see above: influence of the onset flow boundary layer, asymptotic behavior of the ramp pressure), with the benefit of smaller thermal loads. We note in this context, that a large aspect ratio of the flap reduces flow three-dimensionality and associated losses in effectiveness.

6.6.4 Volumes of Stabilization and Control Surfaces

The so-called volume of a stabilizer or control surface—plan area (size) times moment arm (e.g. distance from mid chord of control surface to center-of-gravity)—is a measure for its overall performance, i.e., the moment it generates. In order to get a feeling for the orders of magnitude of volumes of flight vehicles in this regard, we consider in Table 6.19 selected geometrical data,[37] and in Table 6.20 the plan areas, moment arms, and volumes of aerodynamic trim, stabilization and control surfaces, of a RV-W (Space Shuttle Orbiter), a CAV (SÄNGER lower stage), and a typical small/medium-range passenger

[36] We point in this regard to the general flight mechanical layout of the vehicle. Reducing the static stability margin, Chapter 7 would reduce the trim moment. With the small lever arms of hypersonic vehicles, in contrast to classical aircraft, this still means a rather large trim force and hence a considerable trim drag. A reduced stability margin, on the other hand, makes a flight vehicle more susceptible to atmospheric and other perturbations.

[37] We choose in each case the volume $V_{ref} = A_{ref} \cdot L_{ref}$ as reference flap volume.

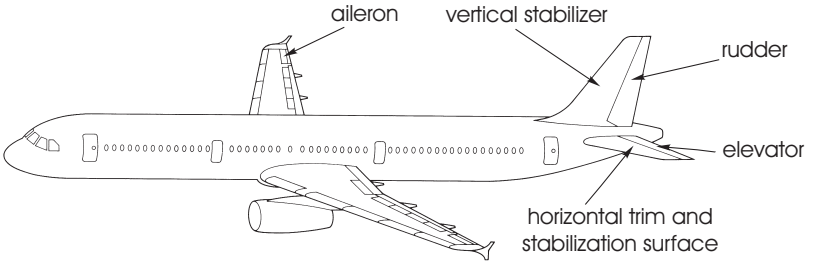

Fig. 6.48. Trim, stabilization, and control surfaces of a typical passenger aircraft.

Table 6.19. Geometrical reference data of a RV-W (Space Shuttle Orbiter [54]), a CAV (SÄNGER lower stage [55]) and a typical small/medium-range passenger aircraft: plan area, length, half span, reference flap volume, and the chosen x-reference position of the center-of-gravity. The center-of-gravity position given for the SÄNGER lower stage is that of the TSTO-system just before upper stage launch.

Reference data	RV-W vehicle	CAV vehicle	Small/medium-range passenger aircraft
Area A_{ref} [m^2]	361.3 total plan area	1,435.0 total plan area	122.0 wing plan area
Length L_{ref} [m]	32.77	82.5	38.0
Half span s_{ref} [m]	11.92	22.55	17.0
Reference flap volume $V_{ref} = A_{ref}L_{ref}$ [m^3]	11,841.10	118,387.50	4,636.0
center-of-gravity reference position x_{cog}/L_{ref}	0.66	0.74	0.43

aircraft. For the latter we show a typical configuration in Fig. 6.48, which exhibits nicely the large moment arms, hence volumes, which the different aerodynamic trim, stabilization and control surfaces have. The center-of-gravity lies at $x/L \approx 0.43$.

Regarding the Space Shuttle Orbiter, Figs. 3.2 and 3.40, we give the data in relation to the plan area $A_{ref} = 361.3$ m^2 (usually the wing area alone, 249.91 m^2, is used as the reference surface for force and moment coefficients), the vehicle length up to the body flap, and the half span [54]. For the SÄNGER lower stage, Fig. 3.2, we give the data in relation to the plan area, the vehicle length, and the half span [55]. For the passenger aircraft we take the wing area as reference area, the fuselage length as reference length, and also the wing half span.

The selected data in Table 6.20 for the RV-W's and CAV's are partly estimated. Since we are here interested in the relations of the volumes only, we do not look at the whole problem of flyability and controllability of the vehi-

cles, also not at pitch, roll, and yaw damping. We also do not regard that, for instance, in the case of the Space Shuttle Orbiter, Sub-Section 2.1.2, the RCS is active in pitch for altitudes down to $H \approx 70$ km, the rudder becomes active only at flight Mach numbers $M_\infty < 5$ and that the RCS in yaw is active down to $M_\infty \approx 1$. Concerning the SÄNGER lower stage, we disregard the influence of the thrust vector on the longitudinal motion, Sub-Section 2.2.3. We also note, that the configuration at the end of the German Hypersonic Technology Programme was still a preliminary one. The demands from the side of flyability and controllability were not yet taken fully into account. The values in Table 6.20 do not say all. They must be seen in view of the issues of stable and controlled flight, e.g., (longitudinal) trim, longitudinal and lateral stability, moments of inertia around the three axes, angular turn rates, and damping properties. Therefore we contrast them only with the (estimated) data of the typical small/medium-range passenger aircraft.

We observe in summary that the volume of the longitudinal trim and stabilization device of the passenger aircraft is roughly one order of magnitude larger than that of RV-W's and CAV's. The other volumes concerning the longitudinal motion are also significantly larger for the passenger aircraft, mostly simply due to the more forward location of the center-of-gravity. The volumes for roll control are of similar size. All volumes of a CAV are significantly smaller than that of the other ones. This probably is due to the preliminary state of design and because the influence of the propulsion system was not yet taken into account.

Table 6.20 underlines for RV-W's and CAV's, in contrast to large transonic passenger aircraft, the need of high effectiveness of all aerodynamic trim, stabilization and control surfaces which must be ensured despite the harsh aerothermodynamic environment at hypersonic flight. In general, the volume of a stabilization, trim or control surface cannot be enlarged in a simple manner. Two basic possibilities are given: one is to enlarge the plan area, the other to enlarge the moment arm. If the moment arm is fixed, an increase of the plan area would be a way to get a desired performance. This must be considered in connection with the overall layout of the vehicle. If the plan area of a given stabilization or control surface cannot be enlarged, utilization of two surfaces is a possibility. For instance, for vertical stabilizers, and hence also rudders, dual arrangements, Sub-Section 6.6.1, are a typical means to increase their volume in view of moment-arm restrictions. Such means can also be wing-tip fins. For RV-W's, like at the HERMES and the X-38 configurations, wing-tip fins have the other benefit that they are not completely shadowed by the fuselage at the large angles of attack during re-entry flight.

However, such arrangements pose other problems. Dual vertical stabilizers may be prone to structural fatigue problems due to impingement of lee-side vortices of the delta wing. The anyway highly thermally loaded wing-tip fins and rudders [58], must avoid during re-entry the impingement of the bow shock and hence must be wrapped inside the bow shock surface [59]. Otherwise the

Table 6.20. Aerodynamic trim, stabilization and control surfaces of a RV-W-type vehicle (Space Shuttle Orbiter), a CAV-type vehicle (TSTO-system SÄNGER lower stage), and a typical small/medium-range passenger aircraft, and selected relative estimated plan areas, moment arms, and volumes of trim, stabilization and control surfaces. For the reference values, see Table 6.19.

Relative data	RV-W-type vehicle	CAV-type vehicle	Typical small/medium-range passenger aircraft
Longitudinal trim and stabilization devices:	body flap	elevators	horizontal tail plane
Plane area A/A_{ref}	0.035	0.048	0.25
x-moment arm L/L_{ref}	0.38	0.17	0.5
Volume V/V_{ref}	0.013	0.0082	0.125
Pitch control devices:	elevators	elevators	elevators
Area A/A_{ref}	0.098	0.048	0.074
x-moment arm L/L_{ref}	0.27	0.17	0.52
Volume V/V_{ref}	0.026	0.0082	0.038
Lateral stabilization devices:	single vertical tail surface	dual vertical tail surfaces	single vertical tail surface
Area A/A_{ref}	0.11	0.12	0.18
x-moment arm L/L_{ref}	0.32	0.20	0.48
Volume V/V_{ref}	0.035	0.024	0.086
Lateral control devices:	rudder	dual rudders	rudder
Area A/A_{ref}	0.021	0.021	0.055
x-moment arm L/L_{ref}	0.41	0.25	0.51
Volume V/V_{ref}	0.0086	0.0053	0.028
Roll control devices:	ailerons	ailerons	ailerons
Area A/A_{ref}	0.037	0.022	0.035
y-moment arm L/s_{ref}	0.83	0.76	0.86
Volume V/V_{ref}	0.031	0.017	0.03

interaction would reduce effectiveness, and the thermal loads would increase structural weight due to insulation needs.

To extend moment arms in general is not a valid option.[38] A proposal in this regard was the configuration of the British SSTO space transportation vehicle HOTOL (Horizontal Take-Off and Landing) project from 1986. The 63 m long

[38] In contrast to aerodynamic trim and control surfaces, a RCS has fewer restrictions regarding the placement of the individual thrusters.

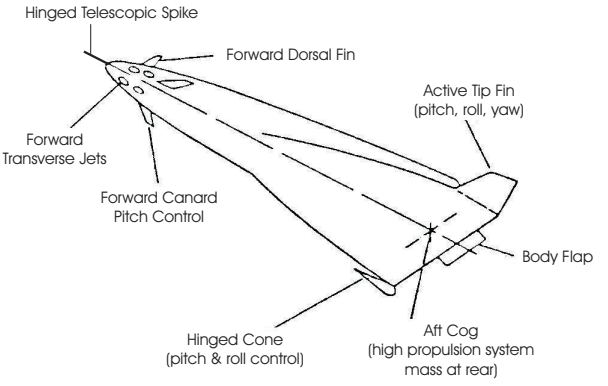

Fig. 6.49. Configuration of the British SSTO project HOTOL from 1986 with unconventional aerodynamic stabilization and control devices at the forward portion of the airframe [60].

ARV-type vehicle was to have a fuselage diameter of 7 m and a delta wing with a span of 28 m. Because the center-of-gravity of the airbreathing propulsion system—with oxygen collection for the rocket cycle above $M_\infty \approx 7$ at $H \gtrapprox 30$ km altitude—was located very far back, Fig. 6.49, an unconventional solution was considered for the placement of the aerodynamic stabilization and control devices [60].

At the aft body a conventional body flap was foreseen and further at the wing-tips "active" fins for pitch, roll, and yaw control as well as hinged cones for pitch and roll control. At the forebody of the vehicle a canard for pitch control, a dorsal fin for yaw stabilization, and an aerospike was proposed, in addition to RCS thrusters. Of course the arrangement near the vehicle nose yields the desired large moment arms. However, the classical weathercock stability for both the longitudinal and the lateral motion is given up. Instead the vehicle is to fly unstable because of the very aft location of the center-of-gravity. This is fundamentally different to the only longitudinal statically unstable hypersonic re-entry flight of the Space Shuttle Orbiter, Sub-Section 3.4.2, because HOTOL is an ascent and return vehicle (ARV) which must cover the whole flight Mach number span from take-off to orbit and back. Unstable flight in principle is possible, as in modern fighter aircraft, but the connected problems of flight control of such a large airbreathing vehicle make the proposal questionable at the moment.

From the side of aerothermodynamics it must be noted that many of the issues of forward located stabilization and control surfaces are not well understood [23]. On the one hand, the surfaces are located in regions with small boundary layer thickness (favorable property of the onset flow), which in principle enhances their effectiveness. On the other hand, the interaction of the flow past these surfaces with the flow field behind them over the vehicle may trip premature laminar–turbulent transition, and induce shock interaction phe-

nomena. Both will cause adverse thermal load increments. A solution as proposed for HOTOL eventually will lead to design and development problems and risks, which should be avoided by all means if possible.

6.7 Concluding Remarks

Effectiveness of trim, stabilization and control devices depends on a number of factors. A major one is their location on the flight vehicle. For aerodynamic control surfaces the optimal onset flow geometry is obvious: two-dimensional onset flow orthogonal to the hinge line. Flight parameters, the vehicle shape and flight attitude govern the resulting entropy layer, the thickness of the onset flow boundary layer, and the inviscid onset flow Mach number.

Experience and the available data base regarding hypersonic flight-vehicle shapes are still small. Detailed ground facility test and computational data, correlated with flight data, are only available for the Space Shuttle Orbiter. It can be dangerous to generalize flight and also ground simulation results found with only one vehicle shape. In any case, different flight vehicle types put different demands on devices, and the involved aerothermodynamic phenomena can be vastly different. In the following sub-sections we summarize important results of this chapter, with a short discussion of ground-simulation issues.

6.7.1 Summary of Results

Important results of the above discussions are listed with selected references, a general review is not intended.

- Effectiveness of aerodynamic trim and control surfaces is governed to a large degree by the onset flow properties, Section 6.2. Important is the optimal onset flow geometry.
- Viscous and high temperature real gas effects have their influence primarily via the onset flow. The vehicle's windward side surface temperature, governed by radiation cooling, has a strong influence on the boundary layer thickness and its separation behavior, Sub-Section 6.2.3.
- The governing similarity parameters are not those of the free-stream but those locally at the edge of the boundary layer. This is important especially for RV-W's where, despite large flight Mach numbers at large angles of attack, the onset flow Mach numbers are small, and Reynolds numbers are relatively high, Sub-Section 6.2.1.
- For RV-W's, boattailing seems to be beneficial for the body flap effectiveness because it increases the onset flow Mach number, Sub-Section 6.3.2. No systematic studies of this effect are known. On the other hand, boattailing introduces a sensitivity to high temperature real gas effects, Sub-Section 3.6.4.
- Space Shuttle Orbiter data indicate that real-gas effects, via the onset flow properties, are the major factor regarding flap effectiveness, Sub-Sec-

tion 6.3.2. This may hold in general for RV-W's and RV-NW's, but not for CAV's and ARV's.

- The increase of the flap deflection angle η in supersonic flow in general increases both the vehicle moment and the hinge moment, and also the moment gradient $C_{m,\eta} = dC_m/d\eta$, Sub-Section 6.3.2.
- The asymptotic pressure plateau on the flap surface is that of the inviscid pressure jump depending on deflection (ramp) angle, onset flow Mach number, and real-gas effects, Sub-Section 6.3.1. This holds at flight altitudes, where the local Reynolds number is not too small and hypersonic viscous interaction is negligible. Space Shuttle Orbiter data suggest that this may hold already at the large speeds and altitudes of the initial re-entry trajectory, even if there, due to the small dynamic pressure, flap effectiveness is very small, and the RCS therefore is active.
- The flap (chord) length should be large enough to make use of the asymptotic pressure plateau, Sub-Section 6.3.1. In general this is no problem, because even at large deflection angles the extent of the separation zone is small. Space Shuttle Orbiter experience shows that in a ground-simulation facility this may be predicted wrongly [31].
- Separation ahead of the hinge line, case c) in Fig. 6.9, and the resulting separation shock, are not necessarily leading to a dramatic decrease of the flap effectiveness, Sub-Section 6.3.2. On the other hand, these effects, which appear—depending on the onset flow Mach number—at large deflection angles, do not enhance flap effectiveness, if the flap length is large enough, such that the asymptotic pressure plateau governs the flap force. The hinge moment in any case may be more strongly influenced than the vehicle pitching moment.
- The hinge moment depends stronger on the flap length than on its width, Section 6.6. It rises quadratically with rising flap length. A large aspect ratio of the control surface reduces losses due to three-dimensional flow effects.
- A small flap length makes larger deflection angles necessary, with the danger that case c) in Fig. 6.9 occurs. In any case, not only the flap effectiveness must be considered, but in conjunction with it also the hinge moment with the resulting actuator performance, weight, volume, and energy demand, Section 6.6.
- Any flap deflection leads to an increase of the thermal loads on the flap, with a considerable enhancement of them around the flap's hinge line, if case c) in Fig. 6.9 is present. Regarding the thermal state of the surface (surface temperature in the presence of radiation cooling and heat flux in the gas at the wall) an asymptotic behavior is observed too, if the flap length is large enough, Sub-Section 6.3.3.
- Non-convex surface radiation effects due to flap deflection seem to play a role more for the onset flow via the surface temperature, [12]. Transverse heat transfer through the flap structure can reduce overall thermal loads,

but if a cavity situation like on the X-38 is given, thermal loads there will increase, Sub-Section 6.3.3.
- The wall shear stress away from the hinge line shows an asymptotic behavior, too, Sub-Section 6.3.4. Its magnitude is important in view of possible surface material erosion effects.
- Experimental and numerical investigations so far concentrate always only on the phenomena present around the flap's hinge line. Because the asymptotic behavior of mechanical and thermal loads on the flap is important for vehicle layout, data are needed to check and validate numerical prediction methods. This concerns especially the prediction of thermal loads in presence of turbulent flow.
- The gap at the hinge line is of concern, because gap flow may influence flap effectiveness. Large gap flow at large deflection angles can reduce or even delete separation around the hinge line, however, with an increase of thermal loads in the gap, Section 6.4. Gaps between neighboring control surfaces decrease effectiveness and locally rise thermal loads.
- On real configurations several 3-D effects can be present. Besides the already mentioned effect of finite flap aspect ratio we can have a sub-optimal onset flow situation, side-wall effects, and interactions with, for instance, the vehicle's bow shock in off-design flight conditions. In all such cases the basic aerothermodynamic phenomena sketched so far will be present, however, modulated accordingly. In general control surface effectiveness is reduced, especially thermal loads can be increased.
- Active control of adverse effects on a flight configuration in general is hardly possible. Layout and optimization of the aerodynamic shape, and the structure and materials concept of the vehicle, as well as the flight trajectory, must take care of such effects. Control means like surface bleed flow applied for inlet ramp flow, Section 4.5.5, are in general not an option for aerodynamic control surfaces.
- Interaction of the jet of a reaction control system with the surface flow, Section 6.5, poses special problems. These are the amplification or de-amplification of the jet effectiveness, the amplification of thermal loads (hot-spots), even at some distance from the jet, and induction of stray forces due to jet impingement. Again it is a matter of overall vehicle layout to fashion and optimize RCS effectiveness and to cope with adverse effects.

6.7.2 Simulation Issues

For general issues of ground facility and computational simulation see, e.g., Sub-Section 9.3.1 [10]. Regarding trim and control devices of hypersonic vehicles the major problem is the characterization of the onset flow properties. With the given shape of the vehicle in a design cycle the accurate and reliable estimation of the effectiveness of a device to a large degree depends on the correct quantification of these properties. This also holds for the quantification of secondary effects, like trim drag, thermal loads increments, etc.

Simulating RV-W's and RV-NW's flight involves the particular problem of high temperature real gas effects. These are vehicle shape dependent, but might be of secondary importance for overall lift and drag (longitudinal motion), if Oswatitsch's independence principle holds, except for the pitching moment, and the lateral motion. Reynolds number, thermal state of the surface (thermal surface effects, [61]) as well as (real-life) surface properties affect the viscous part of the onset flow of a device. The state of the boundary layer is also important.

For CAV's and ARV's (ascent mode) where viscous effects can dominate, Reynolds number, surface temperature, and surface properties play major roles in view of the fact, that the flow predominantly is turbulent, with the location of the transition zone additionally being of large importance. Real-gas effects in general may play a smaller role.

Ground facility simulation now has the problem of simultaneously keeping the relevant scaling laws right, with adequate model sizes and surface properties, as well as with adequate instrumentation. Computational simulation suffers more from deficits of transition and turbulence modelling than from deficits of transport property and high-temperature real-gas models.

When looking at the basic effects and properties of control-device flow, obviously much has been studied, especially regarding the involved strong interaction phenomena. However, building-block experiments in the sense of those discussed in [62] are rare. They should show the asymptotic behavior of the flow parameters on, for instance, a control surface, and at the same time take into account the different domains of similarity parameters, which we have at re-entry vehicles in contrast to airbreathing cruise and acceleration vehicles. Suitable and reliable validation data, including especially minutely reconstructed skin-friction line and velocity field topologies, are needed to improve flow physics and thermodynamic models for computational methods and their validation.

These are the general problems. We have seen, when going into details of design problems as well as building-block experiments, that multidisciplinary simulation issues of large importance arise, too. The radiation-adiabatic temperature is a good approximation of the actual temperature during flight on regular radiation cooled surfaces. In hinge and side gaps of control surfaces, gaps between TPS tiles, between nose caps and tiles, between TPS panels, also at sharp leading edges, this is no more the case, even if non-convex effects are regarded. The reason is that in the wall material temperature gradients normal to the surface, as well as tangentially, occur which can no more be neglected. This concerns generally heat transport by conduction and/or radiation in the structure and the material.

If, for the sake of lightweight design and reduction of design margins, a very accurate prediction of thermal and mechanical loads, besides that of functionality, becomes necessary, this can only be done with the help of multidisciplinary computational simulation. Flow phenomena, and structure and ma-

terial phenomena must be treated in a coupled manner, Sub-Section 8.4.3, in order to describe thermo-mechanical fluid-structure interactions.

Building-block experiments have to overcome a host of challenges. Hot experimental techniques [61], hot model-surface problems (in [63] for instance, thermal wave phenomena on C/C-SiC surfaces in hot air flow are reported), sensor falsification (to be overcome with non-intrusive opto-electronic measurement methods), etc., must be mastered. Today this is possible in laboratory experiments, but the modelling and verification of multidisciplinary simulation and optimization methods makes much more efforts necessary. Finally in-flight testing with dedicated experimental vehicles is required in order to calibrate and verify physical models and data.

6.8 Problems

Problem 6.1. Compute with the relations given in Sub-Section 6.3.1 the incipient separation angle $\eta_{is} \equiv \theta_{is}$ for the laminar flat-plate/ramp flow case from Table 6.8. Use the viscosity relation eq. (10.61).

Problem 6.2. Compute with the relations given in Sub-Section 6.3.1 the incipient separation angle $\eta_{is} \equiv \varphi_{is}$ for the turbulent flat-plate/ramp flow case from Table 6.7.

Problem 6.3. Derive eq. (6.10) from eq. (6.9).

Problem 6.4. Check up to what angles η the proportionality

$$\frac{p_2 - p_1}{p_1} \sim \eta^2$$

gives reasonable results in a) Fig. 6.13 and b) Fig. 6.17. Choose the cases $\gamma_1 = \gamma_{eff} = 1.4$ and take $\eta = 5°$ in each figure as reference point.

Problem 6.5. In Fig. 6.27 we find at the base above the body flap a minimum surface pressure $\log(p/p_0) \approx -1.8$, with $p_0 \equiv p_\infty$. How large is the appendant pressure coefficient c_p? How large is the vacuum pressure coefficient $c_{p_{vac}}$ which was defined in Sub-Section 3.2.3? Is the base pressure close to vacuum?

References

1. Delery, J.M., Marvin, J.G.: Shock Wave/Boundary Layer Interactions. AGARDograph 280 (1986)
2. Dolling, D.S.: Fifty Years of Shock-Wave/boundary layer Interaction Research: What Next? AIAA J. 39(8), 1517–1531 (2001)

3. Knight, D., Yan, H., Panaras, A.G., Zheltovodov, A.: Advances of CFD Prediction of Shock Wave Turbulent Boundary Layer Interactions. Progress in Aerospace Sciences 39, 121–184 (2003)
4. Arnal, D., Delery, J.M.: Laminar-Turbulent Transition and Shock Wave/ Boundary Layer Interaction. RTO-EN-AVT-116, pp. 4-1–4-46 (2005)
5. Simeonides, G.: Hypersonic Shock Wave Boundary Layer Interactions over Simplified Deflected Control Surface Configurations. AGARD-FDP/VKI Special Course, AGARD R-792, pp. 7-1–7-47 (1993)
6. Settles, G.S., Dolling, D.S.: Swept Shock Wave Boundary Layer Interactions. In: Hemsch, M.J., Nielsen, J.N. (eds.) Tactical Missiles Aerodynamics. AIAA Progress in Aeronautics, vol. 104, pp. 297–379 (1986)
7. Panaras, A.G.: Review of the Physics of Swept-Shock/Boundary Layer Interactions. Progress in Aerospace Sciences 32, 173–244 (1996)
8. Smits, A.J., Dussauge, J.-P.: Turbulent Shear Layers in Supersonic Flow, 2nd edn. AIP/Springer, New York (2004)
9. Delery, J.M.: Shock Wave/Turbulent Boundary Layer Interaction and its Control. Progress in Aerospace Sciences 22, 209–280 (1985)
10. Hirschel, E.H.: Basics of Aerothermodynamics. Progress in Astronautics and Aeronautics, AIAA, Reston, Va, vol. 204. Springer, Heidelberg (2004)
11. Wüthrich, S., Sawley, M.L., Perruchoud, G.: The Coupled Euler/Boundary Layer Method as a Design Tool for Hypersonic Re-Entry Vehicles. Zeit-schrift für Flugwissenschaften und Weltraumforschung (ZFW) 20(3), 137–144 (1996)
12. Häberle, J.: Einfluss heisser Oberflächen auf aerothermodynamische Flugeigenschaften von HOPPER/PHOENIX (Influence of Hot Surfaces on Aerothermodynamic Flight Properties of HOPPER/PHOENIX). Diploma Thesis, Institut für Aerodynamik und Gasdynamik, Universität Stuttgart, Germany (2004)
13. Daimler-Benz Aerospace Space Infrastructure, FESTIP System Study Proceedings. FFSC-15 Suborbital HTO-HL System Concept Family. Dasa München/Ottobrunn, Germany (1999)
14. Wilcox, D.C.: Turbulence Modelling for CFD. DCW Industries, La Cañada, CAL, USA (1998)
15. Kliche, D.: Personal communication. München, Germany (2008)
16. Griffith, B.F., Maus, J.R., Best, J.T.: Explanation of the Hypersonic Longitudinal Stability Problem – Lessons Learned. In: Arrington, J.P., Jones, J.J. (eds.) Shuttle Performance: Lessons Learned. NASA CP-2283, Part 1, pp. 347–380 (1983)
17. Marini, M.: Analysis of Hypersonic Compression Ramp Laminar Flows under Sharp Leading Edge Conditions. Aerospace Science and Technology 5, 257–271 (2001)
18. Henze, A., Schröder, W., Bleilebens, M., Olivier, H.: Numerical and Experimental Investigations on the Influence of Thermal Boundary Conditions on Shock Boundary Layer Interaction. Computational Fluid Dynamics J. 12(2), 401–407 (2003)
19. Simeonides, G.: Personal communication (2006)
20. Drougge, G.: An Experimental Investigation of the Influence of Strong Adverse Pressure Gradients on Turbulent Boundary Layers at Supersonic Speeds. FFA Report 47, Stockholm, Sweden (1953)
21. Needham, D.A.: Laminar Separation in Hypersonic Flow. Doctoral thesis, University London, U.K (1965)

22. Korkegi, R.H.: Comparison of Shock-Induced Two- and Three-Dimensional Incipient Turbulent Separation. AIAA J. 13(4), 534–535 (1975)
23. Neumann, R.D.: Defining the Aerothermodynamic Methodology. In: Bertin, J.J., Glowinski, R., Periaux, J. (eds.) Hypersonics. Defining the Hypersonic Environment, vol. 1, pp. 125–204. Birkhäuser, Boston (1989)
24. Elfstrom, G.M.: Turbulent Hypersonic Flow at a Wedge-Compression Corner. J. of Fluid Mechanics 53, Part 1, 113–127 (1972)
25. Edney, B.: Anomalous Heat Transfer and Pressure Distributions on Blunt Bodies at Hypersonic Speeds in the Presence of an Impinging Shock. FFA Rep. 115 (1968)
26. Coratekin, T., van Keuk, J., Ballmann, J.: On the Performance of Upwind Schemes and Turbulence Models in Hypersonic Flows. AIAA J. 42(5), 945–957 (2004)
27. Coleman, G.T., Stollery, J.L.: Heat Transfer from Hypersonic Turbulent Flow at a Wedge Compression Corner. J. Fluid Mechanics 56, 741–752 (1972)
28. Holden, M.S., Moselle, J.R.: Theoretical and Experimental Studies for the Shock Wave-Boundary Layer Interaction on Compression Surfaces in Hypersonic Flow. ARL 70-0002, Aerospace Research Laboratories, Wright-Patterson AFB, Ohio (1970)
29. Simeonides, G., Haase, W.: Experimental and Computational Investigations of Hypersonic Flow About Compression Ramps. J. Fluid Mechanics 283, 17–42 (1995)
30. Reisinger, D., Müller, J., Olejak, D., Staudacher, W.: Effect of Mach Number and Reynolds Number on Flap Efficiencies in the Supersonic Regime. In: Proc. 85th Semi-Annual STA Meeting, Atlanta, GA (1996)
31. Weilmuenster, K.J., Gnoffo, P.A., Greene, F.A.: Navier-Stokes Simulations of Orbiter Aerodynamic Characteristics. In: Throckmorton, D.A. (ed.) Orbiter Experiments (OEX) Aerothermodynamics Symposium. NASA CP-3248, Part 1, pp. 447–501 (1995)
32. Thorwald, B.: Personal communication (2006)
33. Hirschel, E.H.: Heat Loads as Key Problem of Hypersonic Flight. Zeitschrift für Flugwissenschaften und Weltraumforschung (ZFW) 16(6), 349–356 (1992)
34. Bushnell, D.M., Weinstein, L.M.: Correlation of Peak Heating for Reattachment of Separated Flow. J. Spacecraft and Rockets 5, 1111–1112 (196 Radiation Cooled8)
35. Celic, A., Hirschel, E.H.: Comparison of Eddy-Viscosity Turbulence Models in Flows with Adverse Pressure Gradient. AIAA J. 44(10), 2156–2169 (2006)
36. Zeiss, W.: Modelling of Hot, Radiation Cooled Surfaces. TET-DASA-21-TN-2402, Dasa, München/Ottobrunn, Germany (1999)
37. Behr, R.: Hot, Radiation Cooled Surfaces. TET-DASA-21-TN-2410, Dasa, München/Ottobrunn, Germany (2002)
38. Weiland, C., Longo, J.M.A., Gülhan, A., Decker, K.: Aerothermodynamics for Reusable Launch Systems. Aerospace Science and Technology 8, 101–110 (2004)
39. Görtler, H.: Über eine dreidimensionale Instabilität laminarer Grenzschichten an konkaven Wänden. Nachrichten der Gesellschaft der Wissenschaften zu Göttingen, Mathematisch-Physikalische Klasse, Neue Folge, Fachgruppe 1, Bd. 2, pp. 1–26 (1940)
40. Ginoux, J.J.: Streamwise Vortices in Reattaching High-Speed Flows: A Suggested Approach. AIAA J. 9(4), 759–760 (1971)

41. Lüdecke, H., Radespiel, R., Schülein, E.: Simulation of Streamwise Vortices at the Flaps of Re-Entry Vehicles. Aerospace Science and Technology 8, 703–714 (2004)
42. Lüdecke, H.: Computation of Görtler Vortices in Separated Hypersonic Flows. In: Satofuka, N. (ed.) Computational Fluid Dynamics 2000, pp. 171–176. Springer, Heidelberg (2001)
43. Gülhan, A.: Investigation of Gap Heating on a Flap Model in the Arc Heated Facility L3K. TET-DLR-21-TN-3101, DLR/Köln-Porz, Germany (1999)
44. Behr, R., Görgen, J.: CFD Analysis of Gap Flow Phenomena. TET-DASA-21-TN-2403, Dasa München/Ottobrunn, Germany (2000)
45. Mack, A., Schäfer, R., Gülhan, A., Esser, B.: Flowfield Topology Changes Due to Fluid-Structure Interaction in Hypersonic Flow Using ANSYS and TAU. In: Breitsamter, C., Laschka, B., Heinemann, H.-J., Hilbig, R. (eds.) New Results in Numerical and Experimental Fluid Mechanics IV. Notes on Numerical Fluid Mechanics and Multidisciplinary Design, NNFM 87, pp. 196–203. Springer, Heidelberg (2004)
46. Scallion, W.I.: Space Shuttle Reaction Control System – Flow Field Interactions During Entry. In: Throckmorton, D.A. (ed.) Orbiter Experiments (OEX) Aerothermodynamics Symposium. NASA CP-3248, Part 1, pp. 345–370 (1995)
47. Spais, F.W., Cassel, L.A.: Aerodynamic Interference Induced by Reaction Controls. AGARD-AG-173 (1973)
48. Monta, W.J., Rausch, J.R.: Effects of Reaction Control System Jet-Flow Field Interactions on a 0.015 Scale Model Space Shuttle Orbiter Aerodynamic Characteristics. NASA-CR-134074 (1973)
49. Zeiss, W.: Jet/Airflow Interaction. TET-DASA-21-TN-2409, Dasa, München/-Ottobrunn, Germany (2002)
50. Zeiss, W., Behr, R.: Vortical Type Flow with Respect to Jet-External Airflow Interaction. In: Breitsamter, C., Laschka, B., Heinemann, H.-J., Hilbig, R. (eds.) New Results in Numerical and Experimental Fluid Mechanics IV. Notes on Numerical Fluid Mechanics and Multidisciplinary Design, NNFM 87, pp. 188–195. Springer, Heidelberg (2004)
51. Weiland, C.: Typical Vortex Phenomena in Flow Fields Past Space Vehicles. In: Blackmore, D., Krause, E., Tung, C. (eds.) Vortex Dominated Flows, pp. 251–269. World Scientific Publishing, Singapore (2005)
52. Wang, K.C.: Separating Patterns of Boundary Layer Over an Inclined Body of Revolution. AIAA Journal 10, 1044–1050 (1972)
53. Allen, M.F., Romere, P.O.: Space Shuttle Aerodynamics Flight Test Program. In: Throckmorton, D.A. (ed.) Orbiter Experiments (OEX) Aerothermodynamics Symposium. NASA CP-3248, Part 1, pp. 281–298 (1995)
54. Romere, P.O.: Orbiter (Pre STS-1) Aerodynamic Design Data Book Development and Methodology. In: Throckmorton, D.A. (ed.) Orbiter Experiments (OEX) Aerothermodynamics Symposium. NASA CP-3248, Part 1, pp. 249–280 (1995)
55. Hauck, H.: Leitkonzept SÄNGER – Referenz-Daten-Buch. Issue 1, Revision 2, Dasa, München/Ottobrunn, Germany (1993)
56. Edwards, C.L.W., Small, W.J., Weidner, J.P.: Studies of Scramjet/Air-frame Integration Techniques for Hypersonic Aircraft. AIAA-Paper 75-58 (1975)
57. Kafer, G.C.: Space Shuttle Entry/Landing Flight Control Design Description. AIAA-Paper 82-1601 (1982)

58. Herrmann, U., Radespiel, R., Longo, J.M.A.: Critical Flow Phenomena on the Winglet of Winged Reentry Vehicles. Zeitschrift für Flugwissenschaften und Weltraumforschung (ZFW) 19, 309–319 (1995)
59. Perrier, P.C.: Concepts of Hypersonic Aircraft. In: Bertin, J.J., Glowinski, R., Periaux, J. (eds.) Hypersonics. Defining the Hypersonic Environment, vol. 1, pp. 40–71. Birkhäuser, Boston (1989)
60. East, R.A., Hutt, G.A.: Vehicle Geometry Effects on Hypersonic Stability and Control. In: Proc. Symposium on Fluid Dynamics and Space, VKI, Rhode Saint Genese, Belgium (1986)
61. Hirschel, E.H.: Thermal Surface Effects in Aerothermodynamics. In: Proc. 3rd European Symposium on Aerothermodynamics for Space Vehicles, Noordwijk, The Netherlands, ESA SP-426, pp. 17–31 (1999)
62. Marvin, J.G.: A CFD Validation Roadmap for Hypersonic Flows. AGARD CP-514, pp. 17-1–17-16 (1992)
63. Esser, B., Gülhan, A.: Thermal Fluid-Structure Interaction in Different Atmospheres. In: Proc. 5th European Workshop on Thermal Protection Systems and Hot Structures, Noordwijk, The Netherlands, ESA SP-631 (2006)